UNIVERSITAT DE BARCELONA

Facultat de Matemàtiques
i Informàtica

GRAU DE MATEMÀTIQUES

Treball final de grau

Numerical investigation of the transition from conservative to weakly-dissipative dynamics

Autor: Daniel Elebiary

Director: Dr. Arturo Vieiro
Realitzat a: Departament de Matemàtiques i Informàtica

Barcelona, 21 de juny de 2020

Abstract

Sometimes, conservative dynamical systems model an idealization of real-life processes, but non-conservative forces, such as friction, can play an important role in the (long-term) evolution of the system, and hence they must be considered in order to describe the process more accurately. The main goal of this work is to study the transition from conservative to weakly-dissipative dynamics. To this end, we consider the effect of dissipation in area-preserving maps. The structure of the conservative phase space is explained in the first chapter with the help of several numerical illustrations. In the second chapter, we design some numerical experiments in order to investigate some of the properties of the transition to the dissipative regime, along with a general description of this scenario.

Resum

A vegades, els sistemes dinàmics conservatius modelen una idealització de processos reals, però forces no conservatives, com la fricció, poden jugar un paper important en la evolució (a llarg termini) del sistema, i per tant han de ser considerades per tal de descriure el procés més acuradament. El principal objectiu d'aquest treball és estudiar la transició de la dinàmica conservativa a la feblement dissipativa. Per això, considerem l'efecte de dissipació en aplicacions que preserven l'àrea. L'estructura de l'espai de fase conservatiu està explicada al primer capítol amb ajuda de diverses il·lustracions numèriques. Al segon capítol, dissenyem alguns experiments numèrics per tal d'investigar algunes propietats de la transició al règim dissipatiu, juntament amb una descripció general d'aquest escenari.

2010 Mathematics Subject Classification. 37C05, 37C29, 37G35

Acknowledgements

First and foremost, I would like to thank my advisor, Dr. Arturo Vieiro, for accepting me as his pupil and showing me the beauty of this branch of mathematics which I had not delved into during my stay at the faculty. Despite the tough times, he has spent numerous hours on video conferences with me, clearing every doubt I could have and showing me how to proceed when I was lost. I sincerely cannot say to full extent how much I have learnt with him, not only of mathematics, during this six-month period. Thank you, Arturo, for the best university experience anyone could have wished for.

I also want to give thanks to my mom and brother, who have always been there, giving me unconditional love and support, even when I was upset because something was not going the way I wanted to. They are true blessings who are with me in the good times but, most importantly, in the bad. My deepest gratitude goes to them.

I would like to express my gratefulness to the rest of my family and friends, which are always there, even when I am too busy and cannot see or talk to them for long periods of time.

Last, but not least, to my dad. I would not be here without you. From when I was little, you inspired me to be a better person, and instilled your passion for science in me. Wherever you are, know that I strive everyday to become a better person, to take care of the family and to be at a 100% at everything I do. I wish I could share with you the joy that the conclusion of this work brings to me, but I know you are watching from afar. This work is dedicated to you.

Contents

Introduction

Many real-life processes, both deterministic and random, evolve in time, and can be mathematically modelled by either a differential equation or by a discrete map. The study of these constitutes the branch of mathematics known as Dynamical Systems.

In this work, we will study the dynamics of discrete mappings $F : U \subset \mathbb{R}^n \to \mathbb{R}^n$, that is, the behaviour of points $x \in U$ under iterates of F. In particular, we are interested in real *analytic*[1] *area-preserving maps* (APMs), which are mappings $F : \mathbb{R}^2 \to \mathbb{R}^2$ such that $\det(DF(x)) = 1 \ \forall x \in \mathbb{R}^2$, where DF denotes the differential of F. Analyticity has great importance on some phenomena exhibited in the dynamics of APMs, specially in beyond all orders phenomena like the splitting of separatrices, which will be shown in chapter 1.

More precisely, we will consider a uniparametric family of APMs $\{F_\alpha\}_{\alpha\in\mathbb{R}}$. Real-life systems often have parameters, such as the constant of a spring or the mass of an asteroid. One is then interested in the robustness properties of the system. Hence, bifurcations are of particular interest because they produce topological changes of the phase space under small variations of the parameter, affecting the local and global dynamics of F.

Indeed, bifurcations might have a local effect on the dynamics, such as the birth of fixed or periodic points. This dynamics can be studied using Taylor expansions and local analysis tools. On the other hand, global bifurcations produce non-local topological changes. For example, the breakdown of invariant curves allows the invariant manifolds of hyperbolic points to intersect across the phase space.

Nevertheless, we will not restrict ourselves to conservative perturbations. We are specifically interested in dissipative perturbations, e.g. a pendulum with friction. Weakly-dissipative regimes are relevant in concrete applications, like celestial mechanics [7], where the Hamiltonian models, although very accurate, are simply idealizations of the true dynamics. As we will see, the changes on the phase space

[1] Analyticity implies that F is a $\mathcal{C}^r$-diffeomorphism $\forall r \geq 0$ (i.e. its a r-times continuously differentiable bijection) and that, when considering $F : \mathbb{R}^2 \subset \mathbb{C}^2 \to \mathbb{C}^2$, the Taylor series of F about any point in its domain has positive radius of convergence.

in the dissipative regime are far more drastic than the ones observed under conservative perturbation: Most invariant curves disappear and the long-term dynamics is condensed in attractors, which are stable invariant objects.

More precisely, we are interested in the transition from the conservative case to the dissipative regime. More specifically, we will analyze and describe this transition by means of numerical experiments. To that end, some specific models are introduced in order to perform simulations.

Hamiltonian systems and APMs

APMs are important because they naturally arise as Poincaré maps of *Hamiltonian systems*. A system is called Hamiltonian (non-autonomous, canonical) if it is of the form

$$\frac{dx}{dt} = \frac{\partial H}{\partial y}(t,x), \qquad \frac{dy}{dt} = -\frac{\partial H}{\partial x}(t,x), \tag{1}$$

for a suitable function $H : \mathbb{R} \times \mathbb{R}^{2n} \to \mathbb{R}^{2n}$. In such a case, we say that the system has $n + 1/2$ degrees of freedom (d.o.f.). If one considers a Hamiltonian function which is periodic in time, the stroboscopic Poincaré map is an APM. In general, however, these APMs do not have an analytical expression.

On the other hand, if one considers an autonomous $2-$d.o.f. Hamiltonian system, then the Hamiltonian function is a *first integral* since

$$\frac{dH}{dt} = \frac{\partial H}{\partial x}\frac{dx}{dt} + \frac{\partial H}{\partial y}\frac{dy}{dt} \overset{(1)}{=} 0, \tag{2}$$

and the system is *conservative*. Therefore, the motion takes place within a 3-dimensional manifold of constant energy level. If one considers a Poincaré section (local, in general, and transversal to some specific recurrent motion inside the energy level, such as a periodic orbit), then one obtains an APM again.

We refer to [1] for details on the derivations and proofs of the previous statements.

The dynamics of an APM (and, in general, of any dynamical system) is organized around *invariant objects* of the phase space. The simplest invariant object is a fixed point, which is a point $p \in \mathbb{R}^2$ such that $F(p) = p$. Other invariant objects are periodic orbits and invariant curves with quasiperiodic motion, which together with their invariant manifolds (if they have) form the *skeleton* of the APM.

Let p be a fixed point of an APM. Then, Spec $DF(p) = \{\lambda, \lambda^{-1}\}$. p is said to be *hyperbolic* if $|\lambda| \neq 1$. In this case, the dynamics of F around p is topologically conjugated to those of the related linear system: This is the content of Hartman-Grobman's theorem [26]. If $|\lambda| = 1$, however, the linear system does not tell the

dynamics of F around p. In this case, $\lambda = e^{i\alpha}$: If $\alpha \neq 0, \pi$, the point is *elliptic*. Otherwise, we will say p is *parabolic*.

As a paradigmatic example of an APM, we will use the Hénon map [14]

$$H_\alpha : \begin{pmatrix} x \\ y \end{pmatrix} \mapsto R_{2\pi\alpha} \begin{pmatrix} x \\ y - x^2 \end{pmatrix}, \qquad \alpha \in (0, 1/2), \tag{3}$$

where $R_{2\pi\alpha} = \begin{pmatrix} \cos(2\pi\alpha) & -\sin(2\pi\alpha) \\ \sin(2\pi\alpha) & \cos(2\pi\alpha) \end{pmatrix}$ is the rotation of angle $2\pi\alpha$.

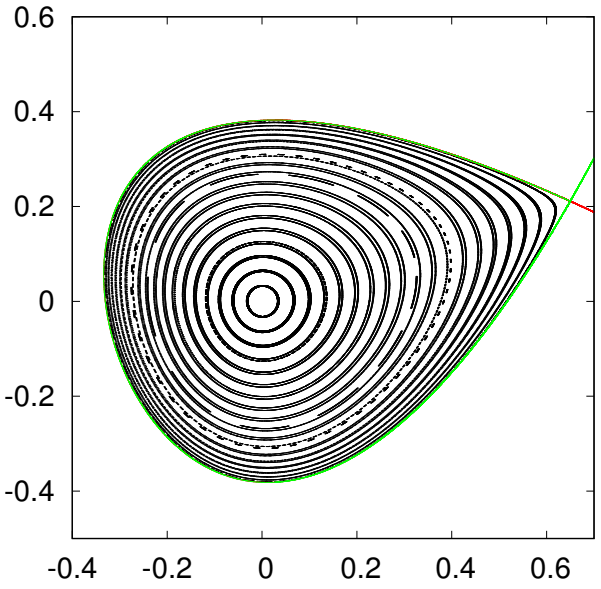

Figure 1: Phase space of H_α for $\alpha = 0.1$.

In figure 1 we display the dynamics on the *phase space* of the Hénon map for $\alpha = 0.1$. It has two fixed points: One elliptic at the origin, and a hyperbolic point near $(0.6, 0.2)$. Observe that there are *invariant curves* and *periodic orbits* surrounding the origin, and these are more deformed the further they are from the origin. As the parameter increases, the existence and persistence of these invariant objects will depend on the *rotation number* of the orbit, an invariant of the homeomorphisms of the circle [2]. If it is irrational enough (in a sense elaborated later), the invariant curve will survive: This is the content of the Moser Twist Theorem [21]. If it is rational, the Poincaré-Birkhoff theorem [2] states (under certain conditions) that there exist two periodic orbits with the same period. We shall summarize these theoretical results in chapter 1.

Further away from the origin, the saddle has an *unstable* and *stable* invariant manifold which enclose the *stability region*. Even though they seem coincident,

they are not, and they split further apart the larger the parameter is. This results in *homoclinic* intersections, which give rise to *chaos*. We present the horseshoe dynamics and its relation with transversal homoclinic intersections given by the Birkhoff-Smale theorem [18] in section 1.3.

We will also study the Chirikov standard map [8], which is an area-preserving map defined on the cylinder $\mathbb{S}^1 \times \mathbb{R}$ and given by

$$S_k : \begin{pmatrix} x \\ y \end{pmatrix} \mapsto \begin{pmatrix} \bar{x} \\ \bar{y} \end{pmatrix} = \begin{pmatrix} x + \bar{y} \\ y + \frac{k}{2\pi} \sin 2\pi x \end{pmatrix}, \qquad k \in \mathbb{R}. \tag{4}$$

For $k = 0$, the standard map is an example of *integrable twist map*. The loss of integrability when $k > 0$ produces changes on the phase space which we will study. As k increases, more and more invariant curves break down. The parameter at which the last rotational invariant curve disappears is known as the *Greene parameter* [11]. For larger values of k, points can diffuse along the cylinder.

The reason behind using these two APMs is because they exhibit similar behaviour to that of more complicated APMs (they are universal models), with the advantage that these have an explicit and easy analytical expression, which is quadratic in (3) and contains a trigonometric function in (4). Furthermore, these maps are reversible, and as a consequence the corresponding phase spaces exhibit symmetries.

Weakly-dissipative systems

Now, we discuss how to add dissipation on a conservative dynamical system. There are multiple ways of adding dissipation, each producing different dynamics. We shall consider two kinds of dissipation: A radial one on the plane [23], acting on map (3)

$$H_{\alpha,\epsilon}(x, y) = (1 - \epsilon) H_\alpha(x, y), \qquad 0 < \epsilon \ll 1, \tag{5}$$

and a vertical dissipation on the cylinder [4] acting on map (4)

$$S_{k,\epsilon,\omega} : \begin{pmatrix} x \\ y \end{pmatrix} \mapsto \begin{pmatrix} \bar{x} \\ \bar{y} \end{pmatrix} = \begin{pmatrix} x + \bar{y} + \omega \\ (1 - \epsilon) y + \frac{k}{2\pi} \sin 2\pi x \end{pmatrix}, \qquad k, \omega \in \mathbb{R},\ 0 < \epsilon \ll 1. \tag{6}$$

Radial dissipation on the Hénon map causes elliptic points to turn into *attractors*, invariant objects to which points tend to. Since the dissipation is pointed towards the origin, the elliptic point there will be the attractor capturing the majority of points or, equivalently, the one with the biggest basin of attraction. Nevertheless, there will be a coexistence of attractors for a small dissipation parameter ϵ, where some phase space structures related to the resonances of the conservative

case might survive. These other attractors will be periodic orbits, and it is interesting to see which attractor captures more points. To this end, in chapter 2 we carry out an experiment consisting in iterating initial conditions on an invariant curve from the conservative case surrounding the 1:5 resonance, and see the ratio of points captured by the attractor at the origin in contrast to the periodic attractor for different values of ϵ.

Hyperbolic points and their invariant manifolds also evolve with the dissipation: As ϵ increases, the stable and unstable manifolds of these points separate from one another. This means that, when ϵ is large enough, no homoclinic points survive, and the invariant manifolds become flow-like (like the ones of a pendulum with dissipation). Additionally, invariant manifolds play an important role in guiding orbits through the phase space to one attractor or another. We shall analyze the evolution of invariant manifolds as a function of ϵ in section 2.1.

On the other hand, invariant curves cannot persist under radial dissipation, since the area enclosed by them would be preserved, contrary to the fact that the system is dissipative with constant jacobian, see chapter 2.

For the standard map, however, the dissipation applied on (6) produces different effects than those commented for (5). Since the phase space of the standard map is the cylinder, a single rotational invariant curve does not enclose an area on the phase space, and consequently it can survive under dissipation. On the other hand, as in (5), elliptic points turn into attractors, there is coexistence of attractors for a range of values of the dissipative parameter and the invariant manifolds of the hyperbolic points also evolve and play a role in guiding orbits.

This dissipation is pointed towards $y = 0$, where we expect the attractor capturing most points to be. Moreover, variation of k, ϵ and ω causes an interesting effect: The attractor can now be an invariant curve, a periodic orbit or a *strange attractor*. To support this, we will show numerical evidences of the existence of periodic strange attractors of Hénon type [15].

The aim of our study of the dissipative standard map is to see the evolution of the attractor for different values of the aforementioned parameters, including the study of the breakdown of the attracting invariant curve, and the existence of periodic attractors and strange attractors with periodic components.

Contents of this work

As mentioned above, the main goal of this work is to study the effect of specific dissipative perturbations on APMs. To better understand the dynamics, we first study the conservative case, in order to know the structure of the phase space and its transition into the dissipative case. The summarized contents of the chapters

are:

Chapter 1. It is a descriptive chapter where we present the main aspects of the dynamics of APMs around an elliptic fixed point. The contents of the chapter are developed in order to explain what is observed in the phase space of the Hénon map and the standard map. It has a section of basic notions, including results (without proofs) on the dynamics of APMs around hyperbolic fixed points, and another section including results on the dynamics around an elliptic fixed point, including normal forms, twist maps, the Moser Twist theorem, the Poincaré-Birkhoff theorem and the horseshoe map.

Chapter 2. It addresses the effect of different dissipations for the maps considered in the previous chapter. In particular, its main aim is to see how the conservative structure is mostly destroyed, and how some remaining elements evolve under dissipation: Invariant curves are (in general) broken down, elliptic points become attractors and the invariant manifolds of the saddles become flow-like. In this chapter, we present numerical experiments to discuss the transition to a weakly-dissipative regime. Concretely, we have performed the following simulations:

- For the Hénon map, the main objective is to study the coexistence of attractors through an experiment whose purpose is to know how many points are captured by each attractor after iteration.
- For the standard map, different kinds of attractors occur for different values of the parameters. The goal is then to see how the main attractor evolves when changing parameters.

Chapter 3. The conclusions of the work are displayed here, summarizing our main results. Moreover, it poses some questions which could lead to future work.

Chapter 1

Overview of area-preserving maps

Many fields of study require the analysis of data evolving in time. For this purpose, we introduce *dynamical systems*, systems whose states change in time. In this work, we deal with finite deterministic dynamical systems. Furthermore, unless stated otherwise, we consider analytic dynamical systems of one of the following types:

1. **Discrete dynamical system:** Those whose time variable t is discrete ($t \in \mathbb{Z}$). They can be presented by the iteration of a function $F : U \subset \mathbb{R}^n \to \mathbb{R}^n$
$$x_t \mapsto x_{t+1} = F(x_t). \tag{1.1}$$
2. **Continuous dynamical system:** Those with a continuous time variable ($t \in \mathbb{R}$ or $t \in \mathbb{C}$). Their time evolution is given by a differential equation, which for our purpose will be an ordinary differential equation (ODE)
$$\dot{x} = f(t, x), \tag{1.2}$$
where $f : I \times \mathrm{U} \to \mathbb{R}^n$.

In (1.1) and (1.2), x is a *state* of the system, which takes values in the *phase space* U, which can be the Euclidean space or a subspace thereof, or a non-Euclidean *differentiable manifold* such as the the cylinder.

Both kinds of dynamical systems are related. In fact, when studying a discrete system, it is often useful to relate it to a suitable continuous system. This is called the *suspension* of the map: It uses interpolation to create a non-autonomous time-periodic vector field that is coincident with the map iterates whenever one considers the flow at integer times. Moreover, one can use Hermite's interpolation to ensure the derivatives of the flow are also coincident with the derivatives of the map at those points. This way, we can achieve a flow that is a C^r-diffeomorphism $\forall r$. In general, however, it will not be analytic.

On the other hand, to study the dynamics of a continuous system with flow ϕ we can consider the *time-τ map*: Fixed $\tau \in \mathbb{R}$, $x \mapsto y = \phi_\tau(x)$. Another way is to

consider the Poincaré section Σ (a codimension 1 surface in U where the flow is locally transverse) and define a *Poincaré map*: $x \in \Sigma$ is mapped to $y \in \Sigma$ iff exists $t_x \in \mathbb{R}$ such that $\phi_{t_x}(x) = y$ and $\phi_t(x) \notin \Sigma \ \forall t < t_x$.

As we have stated in the introduction, this work focuses on the study of analytic area-preserving maps under dissipation. The purpose of this chapter is to show and explain the dynamics of analytic APMs in the conservative case. This chapter is inspired on [2, 24], but we complement these references with some results and illustrations that ought to facilite the understanding of the topic.

1.1 Basic notions of dynamics

Let $F : \mathbb{R}^2 \to \mathbb{R}^2$ be an analytic APM, that is, a map F such that
- $\det DF(x, y) = 1 \quad \forall (x, y) \in \mathbb{R}^2$.
- F is a real analytical diffeomorphism.

For $m \in \mathbb{Z}^+$, F^m is the composition of F with itself m times. Since F is a diffeomorphism, its inverse F^{-1} exists. Thus, F^{-m} is the composition of F^{-1} with itself m times, and $F^0 = \mathbf{Id}_{\mathbb{R}^2}$. Three important concepts arise from this:

Definition 1.1.1.

1. For each $x \in \mathbb{R}^2$, the *orbit* of x under F is the set $\mathcal{O}(x) = \{F^m(x) \mid m \in \mathbb{Z}\}$.
2. A point $x_* \in \mathbb{R}^2$ is a *fixed point* of F if $F(x_*) = x_*$.
3. A point $x_* \in \mathbb{R}^2$ is a *periodic point* of F if there exists $m \in \mathbb{N}$ such that x_* is a fixed point of F^m.
4. A set $M \subset U$ is *invariant* under F if $F^m(x) \in M \ \forall x \in M$, $\forall m \in \mathbb{Z}$. We write $F(M) \subset M$. If $m \in \mathbb{Z}^+$ ($m \in \mathbb{Z}^-$), we say M is *positively (negatively) invariant*.

The minimum value of m satisfying $F^m(x_*) = x_*$ is called the *period* of x_*, and the orbit $\{x_*, F(x_*), \ldots, F^{m-1}(x_*)\}$ is called *periodic orbit of period m* or *m-cycle*. In addition, all points in an m-cycle are periodic points of period m, and a fixed point is a periodic point of period 1.

Fixed points and periodic orbits are invariant compact sets. As we commented in the introduction, the dynamics of a system is organised around these invariant objects in what is called the *skeleton* of the system.

Another important feature of APMs is that they can be *reversible* under certain mappings known as *reversors*.

Definition 1.1.2.

1. A map $R : \mathbb{R}^2 \to \mathbb{R}^2$ is called an *involution* if it is its own inverse, that is,

$$R(R(x)) = x \quad \forall x \in \mathbb{R}^2. \tag{1.3}$$

2. An involution $R : \mathbb{R}^2 \to \mathbb{R}^2$ is a *reversor* for a $\mathcal{C}^r$-diffeomorphism $F : \mathbb{R}^2 \to \mathbb{R}^2$, $r \geq 0$, if

$$R \circ F \circ R(x) = F^{-1}(x) \quad \forall x \in \mathbb{R}^2. \tag{1.4}$$

Reversibility implies that the APM will be symmetric with respect to a certain curve, which is in fact the set of fixed points of the reversor. This feature will help in plotting the invariant manifolds of hyperbolic fixed points, which is explained at the end of this section. Moreover, reversibility plays an important role in finding the periodic points of reversible mappings. This is the content of proposition 1.1.1.

Proposition 1.1.1. *Let R be a reversor for a mapping F with fixed point set $Fix(R) = \{x \in \mathbb{R}^2 \,|R(x) = x\}$. Let $x_* \in Fix(R)$. If there exists $m \in \mathbb{N}$ such that $F^m(x_*) \in Fix(R)$ and $F^n(x_*) \notin Fix(R)$ $\forall n < m$, then x_* is a periodic point of F. Furthermore, either x_* has period m or it has period $2m$.*

Proof. $F^m(x_*) \in Fix(R) \Leftrightarrow R(F^m(x_*)) = F^m(x_*)$. Since $x_* \in Fix(R)$, we can write the left hand side of the equation as $R(F^m(x_*)) = R(F^m(R(x_*))) \overset{(1.4)}{=} F^{-m}(x_*)$. Thus, $F^{-m}(x_*) = F^m(x_*) \Leftrightarrow F^{2m}(x_*) = x_* \Rightarrow x_*$ is a periodic point of F. As for the periodicity of x_*:

- If $F^m(x_*) = x_*$, then x_* is m-periodic. Indeed, if there exists $n < m$ such that $F^n(x_*) = x_*$, then $R(F^n(x_*)) = R(x_*) = x_* = F^n(x_*)$, which contradicts the hypothesis that m is the least natural number satisfying $F^m(x_*) \in Fix(R)$.
- If $F^m(x_*) \neq x_*$, then x_* is $2m$-periodic because, if there existed $n < 2m$ such that $F^n(x_*) = x_*$, then n would divide $2m$, which would imply either $n|m$ or $n|2$. In the former, $F^m(x_*) = x_*$ contradicting the hypothesis. In the latter, either $n = 1$ or $n = 2$. In both cases, arguing in the same manner as above, we arrive at a contradiction.

□

Remark. The main consequence of this proposition is that if we iterate F picking initial conditions along $Fix(R)$ for some reversor R of F, we will be able to obtain the periodic points of F with period up to twice the number of iterates.

We will study area-preserving maps using the Hénon map (3) as an example. As noted in [14], it is the simplest APM with non-trivial behaviour, making it a good model for numerical simulations.

The phase space of the Hénon map is depicted in figure 1.1 for the value $\alpha = 0.21$. This map has a fixed point p_e at the origin and another one at $p_h = (2\tan\pi\alpha, 2\tan^2\pi\alpha)$. These behave differently, however, which is apparent from looking at the figure again: The dynamics concentrates around the fixed point at the origin. Meanwhile, the other fixed point seems to be at the edge of the domain

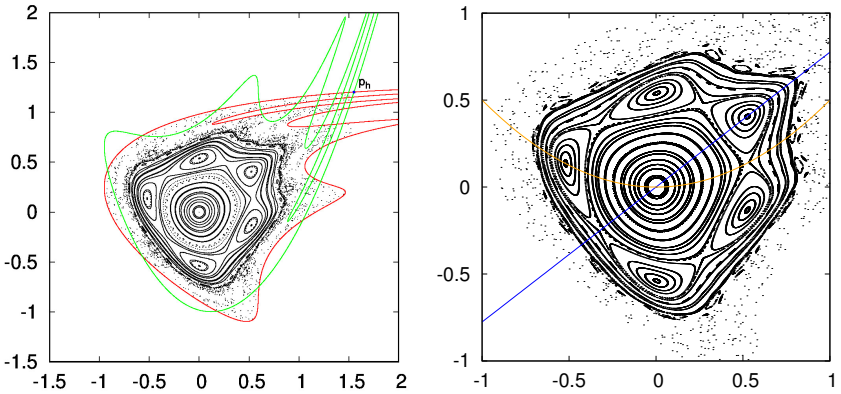

Figure 1.1: **Left:** Phase space of H_α for $\alpha = 0.21$. The hyperbolic fixed point is plotted in blue, whereas its stable and unstable manifolds are depicted in green and red, respectively. **Right:** Close-up of the phase space around the elliptic fixed point. The symmetry lines are plotted in blue and orange.

where the invariant and recurrent dynamics occurs. The Hénon map is reversible by means of the involutions

$$(x, y) \mapsto (\cos(2\pi\alpha)x + \sin(2\pi\alpha)y, \sin(2\pi\alpha)x - \cos(2\pi\alpha)y), \tag{1.5}$$

$$(x, y) \mapsto (x, x^2 - y), \tag{1.6}$$

which have $y = \tan(\pi\alpha)x$ and $y = x^2/2$ as symmetry lines, respectively. These intersect at the fixed points of the mapping, and are plotted on the right of figure 1.1 in blue and orange, respectively.

The following definitions will help us classify fixed and periodic points depending on the behaviour of the orbits close to them. Let x_* be a fixed point of an APM F. In addition, let $DF(x_*)$ be the differential of F evaluated at x_*. For an APM, one has Spec $DF(x_*) = \{\lambda, \lambda^{-1}\}$.

Definition 1.1.3. A fixed point x_* is said to be *hyperbolic* if $\lambda \neq 1\ \forall \lambda \in$ Spec $DF(x_*)$. In particular, x_* is *linearly stable (unstable)* if $\lambda < 1$ $(\lambda > 1)$ $\forall \lambda \in$ Spec $DF(x_*)$, and it is called a *saddle* otherwise.

Fixed points which do not satisfy definition 1.1.3 are called *non-hyperbolic*. In particular, they have all eigenvalues with modulus equal to unity. We say a non-hyperbolic fixed point is *elliptic* if $\lambda = e^{2\pi i\alpha}$, $\alpha \neq 0, 1/2$, and *parabolic* otherwise. In both cases, we say that λ is the *multiplier* of the fixed point. An important trait of the Hénon map is that any APM having an elliptic fixed point can be reduced to the Hénon map in a neighbourhood of this point [14].

In addition, we can generalize the concept of hyperbolic and elliptic fixed points to periodic points: An m-periodic point x_* is hyperbolic (resp. elliptic) if x_* is a hyperbolic (resp. elliptic) fixed point of F^m. In particular, all results yielded for hyperbolic (resp. elliptic) fixed points will be valid for periodic hyperbolic (resp. elliptic) points considering the appropriate power of F.

For the Hénon map, p_e is elliptic, with eigenvalues $\lambda = e^{2\pi i\alpha}$ and $\bar{\lambda}$, whereas p_h is saddle-type hyperbolic with eigenvalues $\lambda = c + 2st + \sqrt{(c+2st)^2 - 1} > 1$ and $\lambda^{-1} < 1$, where $c = \cos(2\pi\alpha)$, $s = \sin(2\pi\alpha)$ and $t = \tan(\pi\alpha)$. A more general sense of stability is given in the following definition.

Definition 1.1.4. A fixed point x_* is said to be *(Lyapunov) stable* if, for every neighbourhood N of x_*, there is a neighbourhood $M \subset N$ of x_* such that if $x \in M$ then $f^m(x) \in N \; \forall m > 0$. Moreover, x_* is said to be *assymptotically stable* if $f^m(x) \overset{m\to\infty}{\to} x_*$.

Hence, a fixed point x_* is Lyapunov stable if iterates of points "near" it remain "near" it, and it is assymptotically stable if the iterates of points "near" x_* tend to the fixed point. If x_* Lyapunov stable but not assymptotically stable, it is *neutrally stable*. If x_* is not stable, it is called *unstable*.

Remark.

1. If a fixed point x_* is linearly stable, then x_* is Lyapunov stable. However, the converse is not true.
2. If x_* is an elliptic fixed point, then it is neutrally stable.

1.1.1 Dynamics around a hyperbolic fixed point

Since the dynamics of APMs is far richer in a neighbourhood of an elliptic point than around a hyperbolic fixed point, we will first study how the latter affects the dynamics around it, and then proceed to do the same with the former. Indeed, the type of dynamics of an APM around a hyperbolic fixed point is determined by the one of the related linear system $DF(p_h)$, which is the content of Hartman-Grobman's theorem [26].

Theorem 1.1.1 (Hartman-Grobman)**.** *Let x_* be a hyperbolic fixed point of the diffeomorphism $F : U \to \mathbb{R}^2$, $U \subset \mathbb{R}^2$ an open subset. Then there is a neighbourhood $N \subset U$ of x_* and a neighbourhood $N' \subset \mathbb{R}^2$ containing the origin such that $F|_N$ is* topologically conjugated *to $DF(x_*)|_{N'}$.*

Two diffeomorphisms $f, g : \mathbb{R}^2 \to \mathbb{R}^2$ are said to be *topologically conjugated* if there is a homeomorphism $h : \mathbb{R}^2 \to \mathbb{R}^2$ such that

$$h \circ f(x,y) = g \circ h(x,y) \quad \forall (x,y) \in \mathbb{R}^2. \tag{1.7}$$

Topological conjugacy sends orbits of f to orbits of g preserving orientation, it respects the fixed point types and sends m-periodic orbits of f to m-periodic orbits of g.

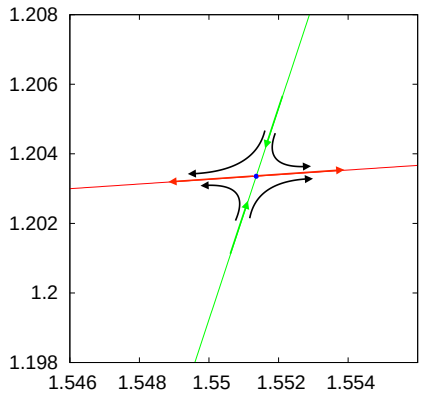

Figure 1.2: Schematical dynamics of $DH_\alpha(p_h)$, $\alpha = 0.21$, around p_h (in blue).

The dynamics of $DH_\alpha(p_h)$ is displayed in figure 1.2. The line in green (resp. red) is the invariant *stable (resp. unstable)* eigenspace, denoted E^s (resp. E^u). Moreover, $DH_\alpha(p_h)|_{E^s}$ (resp. $DH_\alpha(p_h)|_{E^u}$) is a contraction (resp. expansion) and $E^s \oplus E^u = \mathbb{R}^2$. Then, we identify E^s (resp. E^u) with the eigenspaces of eigenvalues with modulus less (resp. greater) than 1. In addition, the sum of both eigenspaces gives the whole of $\mathbb{R}^2$ since each eigenvalue is associated to either E^s or E^u.

Thus, the dynamics of $DH_\alpha(p_h)$ is quite simple: Points belonging to the stable (resp. unstable) eigenspace get closer (further) to p_h as we iterate the mapping. As for the points outside these eigenspaces, they follow the stable eigenspace until they are close to p_h. Then, they follow the unstable eigenspace and go to infinity.

Theorem 1.1.1 tells us that the dynamics of H_α close to p_h is that described above. Nevertheless, the Hénon map is not linear, and points eventually escape the domain where theorem 1.1.1 applies. In figure 1.1 we can see how near p_h the lines depicted in green and red take the roles of the stable and unstable eigenspaces, respectively. The following result extends the notions of stable and unstable subspaces to a non-linear mapping in the form of *invariant manifolds*.

Theorem 1.1.2 (Invariant Manifold)**.** *Let $F : U \to \mathbb{R}^2$ be an analytic APM with a hyperbolic fixed point at $x_* \in U$. Then on a sufficiently small neighbourhood $N \subset U$ of x_*, there exist unique and analytic local* stable *and* unstable manifolds

$$W^s_{loc}(x_*) = \{x \in U | f^m(x) \to x_* \text{ as } n \to \infty\},$$
$$W^u_{loc}(x_*) = \{x \in U | f^m(x) \to x_* \text{ as } n \to -\infty\}$$

of the same dimensions as E^s and E^u for $DF(x_*)$ and tangent to them at x_*.

By iteration, one can define *global* stable and unstable manifolds at x_* by

$$W^s(x_*) = \bigcup_{m\in\mathbb{Z}^+} F^{-m}(W^s_{loc}(x_*)), \qquad W^u(x_*) = \bigcup_{m\in\mathbb{Z}^+} F^m(W^u_{loc}(x_*)). \tag{1.8}$$

Thus, the lines in red and green in figure 1.1 correspond to the unstable and stable manifolds of p_h, respectively. Notice how these have separated with respect to figure 1, where they seemed to be coincident. Since they cannot intersect with themselves and each lobe must have the same area as its successive images, the branches of each manifold surrounding the elliptic point accumulate along the branches which go to infinity, making each successive lobe longer along the direction of the branches, and thinner along the perpendicular direction. In fact, this is a consequence of the λ-lemma [12, 19].

Lemma 1.1.3 (λ-Lemma)**.** *Let $x_* \in U$ be a hyperbolic point of saddle type of an analytic APM $F : U \to \mathbb{R}^2$ having $W^s(x_*)$ and $W^u(x_*)$ as the stable and unstable invariant manifolds, respectively, and let $I \subset W^u(x_*)$ be any interval such that $x_* \in I$. Furthermore, suppose an interval $J \subset W^s(x_*)$ intersects $W^u(x_*)$ transversally. Then, $\bigcup_{n\geq 0} F^n(J)$ contains a sequence intervals acummulating to I in the $\mathcal{C}^1$ topology.*[1].

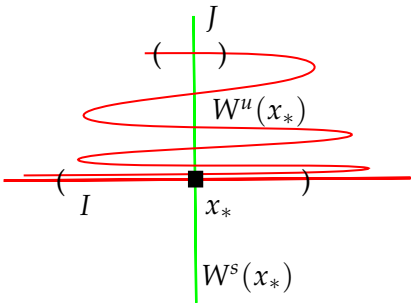

Figure 1.3: Accumulation of the unstable manifold near the hyperbolic point.

The invariant manifolds contribute to the complexity of the dynamics of H_α by intersecting with one another. In, general, if p_h and q_h are two hyperbolic points of an APM F, we say a point p is a *heteroclinic point* if $p \in W^u(p_h) \cap W^s(q_h)$. If $p_h = q_h$, p is a *homoclinic point*. If these manifolds intersect at a non-zero angle, we say p is a *transverse heteroclinic (resp. homoclinic) point*.

Observe that if p is a heteroclinic (resp. homoclinic) point, all points in its orbit are also heteroclinic (resp. homoclinic) points, of which there will be infinitely

[1]This highlights the fact that the two intervals and their derivatives are "close" throughout U. For more information on this statement, see [2, 19].

many by definition (1.8). As a consequence of lemma 1.1.3, these get closer as we approach one hyperbolic point (see figure 1.3). In addition, if one heteroclinic (resp. homoclinic) point is transverse, then all other points in the orbit are as well: This is a consequence of F being a diffeomorphism. These heteroclinic (resp. homoclinic) intersections contribute to the creation of a complicated structure called a *heteroclinic (resp. homoclinic) tangle*, which gives rise to *chaos* [18]. The mechanism through which chaos arises is explained in section 1.3.

The branches of the invariant manifolds surrounding the elliptic point enclose the domain containing all points that do not scape to infinity. This domain, which includes the surroundings of the elliptic point until the last invariant curve as well as the islands in the chaotic region (see section 1.2 for further discussion on these), is known as the *stability domain* of the mapping.

Definition 1.1.5. Given a diffeomorphism $F : U \subset\to \mathbb{R}^n$ and a compact domain $K \subset U$, the *stability domain* of F relative to K is the largest invariant subset of K.

The fact that we can speak about the stability domain of the Hénon map is due to the topology of the invariant manifolds, which form a "fish-like" structure (see figure 1) that implies that, once the iterates leave a compact domain cointaning the loop of the invariant manifolds, all points (except a measure zero set) escape to infinity.

Computation of invariant manifolds

Here we will describe the algorithm used in the computation of the invariant manifolds seen in figures 1 and 1.1. Specifically, we have employed the algorithm in [22], which uses the conjugacy to the linear dynamics along the stable and unstable manifolds associated to a hyperbolic point. Although methods based on higher order parameterizations of the invariant manifolds (we refer to [13] for a full discussion on the topic) allow for more accurate computations, the method sketched here is enough to compute the invariant manifolds displayed in the figures. See A.1 for details on the implementation.

Let $p_h = (x_h, y_h)$ be a hyperbolic fixed point of an APM $F : U \in \mathbb{R}^2 \to \mathbb{R}^2$, and let $\lambda > 1$ be the eigenvalue corresponding to the unstable direction. In order to compute the unstable manifold (for the stable manifold, we apply F^{-1} and $\lambda < 1 \to \lambda^{-1} > 1$), we consider a parametric representation $(x(z), y(z))$ around p_h, with $p_h = (x(0), y(0))$ and $F(x(z), y(z)) \simeq (x(\lambda z), y(\lambda z))$ (consequence of theorem 1.1.1). In particular, we will use the linear parameterization $(x(z), y(z)) = (x_h + zv_1, y_h + zv_2)$, with $v = (v_1, v_2)$ a normalized eigenvector of eigenvalue λ. We proceed as follows:

1. Let z_0 be a value of z such that $||F(x(z), y(z)) - (x(\lambda z), y(\lambda z))||$ is lesser than some tolerance (e.g. 10^{-14}). This ensures the linear approximation is valid. We take the *fundamental domain*[2] generated by z in $[z_0/\lambda, z_0)$.

2. We fix a distance Δs such that successive points (x_{m-1}, y_{m-1}), $(x_m, y_m) \in W^u(p_h)$ should satisfy

$$||(x_{m+1}, y_{m+1}) - (x_m, y_m)|| \leq \Delta s. \tag{1.9}$$

3. Assume we have computed up to (x_m, y_m) satisfying equation (1.9), and we have a current value of z, z_m, and a current value of $\Delta z_m = z_m - z_{m-1}$. We select $\Delta z_{m+1} = \min(1.5, 0.75\frac{\Delta s}{\Delta z_m}) \cdot \Delta z_m$. The factor accompanying Δz_m can be considered a *security factor*.

4. Using $z_{m+1} = z_m + \Delta z_{m+1}$, we perform k iterates, the same number of iterates used to get (x_m, y_m) from z_m, and we obtain (x_{m+1}, y_{m+1}). If $z_{m+1} > z_0$, we divide z_{m+1} by λ and replace k by $k+1$ until z_{m+1} falls in the allowed range.

5. If, despite our choice of z_{m+1}, inequality (1.9) is not verified, we return to step 3 using $0.75\frac{\Delta s}{z_{m+1}}$ as the new security factor.

6. Steps 3 to 5 are repeated until

   (a) we have the desired length of the manifold or
   (b) either Δz_{m+1} or Δz_m are too small. In this case, we must resort to some kind of interpolation to obtain more points of the manifold and continue the algorithm.

Reversibility of the Hénon map allows us to plot the stable manifold as the image of (1.5) of the unstable manifold. As we will see in chapter 2, however, reversibility is often lost when introducing dissipation, and so we will need to use the algorithm described above twice to plot each of the invariant manifolds.

Furthermore, this algorithm does not only allow to compute the invariant manifolds of a fixed point: By considering F^m and the appropiate eigenvalues and eigenvectors, we can also compute the invariant manifolds of an m-periodic hyperbolic point. Nevertheless, along with limited precision, hyperbolicity of these periodic points give numerical problems, increasing the difficulty in the computation of invariant manifolds of these points.

[2]This domain is called fundamental because every orbit in $W^u(p_h)$ has a point (representative) in this domain.

1.2 Dynamics around an elliptic fixed point

As we have seen in figure 1.1, the dynamics of the Hénon map revolves around the elliptic fixed point at the origin. This section is devoted to the understanding the dynamics of APMs around elliptic fixed points. Theorem 1.1.1 does not tell anything about this, and so we must seek an alternative way to explain it. To this end, let $F : \mathbb{R}^2 \to \mathbb{R}^2$ be an APM with a fixed point p (observe we do not ask p to be elliptic yet), which we can assume to be the origin $p = \mathbf{0}$ without loss of generality, and consider the Taylor expansion of F about $\mathbf{0}$

$$F(\mathbf{x}) = DF(\mathbf{0})\mathbf{x} + F_2 + \cdots + F_n + O(|\mathbf{x}|^{n+1}), \tag{1.10}$$

where $\mathbf{x} \in \mathbb{R}^2$ and $F_k \in H^k, k = 2, \ldots, n$, H^k being the vector space of homogeneous polynomials of degree k. Our goal is to eliminate as many terms of order greater than one as possible. If we focus on the term of order $r \geq 2$, we can rewrite equation (1.10) as

$$F(\mathbf{x}) = DF(\mathbf{0})\mathbf{x} + F_r(\mathbf{x}) + O(|\mathbf{x}|^{r+1}). \tag{1.11}$$

We will try to get rid of the term $F_r(\mathbf{x})$ using the polynomial transformation

$$\mathbf{x} = \mathbf{y} + k_r(\mathbf{y}) = K(\mathbf{y}), \tag{1.12}$$

where $\mathbf{y} \in \mathbb{R}^2$, $k_r \in H^r$. If K transforms F into $\tilde{F}$, then

$$\begin{aligned} \tilde{F}(\mathbf{y}) &= K^{-1}(F(K(\mathbf{y}))) = \\ &= DF(\mathbf{0})\mathbf{y} + DF(\mathbf{0})k_r(\mathbf{y}) + F_r(\mathbf{y}) - k_r(DF(\mathbf{0})\mathbf{y}) + O(|\mathbf{y}|^{r+1}). \end{aligned} \tag{1.13}$$

Therefore, we must choose k_r so that

$$k_r(DF(\mathbf{0})\mathbf{y}) - DF(\mathbf{0})k_r(\mathbf{y}) = F_r(\mathbf{y}) \tag{1.14}$$

in order to get

$$F(\mathbf{y}) = DF(\mathbf{0})\mathbf{y} + O(|\mathbf{y}|^{r+1}). \tag{1.15}$$

Equation (1.14) is known as the *homological equation* associated with $DF(\mathbf{0})$. Nevertheless, it is not always possible to chose k_r to get (1.15). It can be seen [2] that the coefficients of $k_r(\mathbf{x})$ can be expressed in terms of the coefficients of $F_r(\mathbf{x})$ as

$$k_{\mathbf{m},i} = \frac{F_{\mathbf{m},i}}{\boldsymbol{\lambda}^{\mathbf{m}} - \lambda_i} \qquad i = 1, 2, \tag{1.16}$$

with $\lambda_1, \lambda_2 \in \text{Spec } DF(\mathbf{0})$, $\mathbf{m} = (m_1, m_2) \in \mathbb{N} \times \mathbb{N}$, $r = m_1 + m_2$ and $\boldsymbol{\lambda}^{\mathbf{m}} = \lambda_1^{m_1}\lambda_2^{m_2}$. Thus, we are not able to eliminate the term of order r if

$$\lambda_i = \boldsymbol{\lambda}^{\mathbf{m}} \tag{1.17}$$

for some allowed $\mathbf{m}$ and $i = 1, 2$. In this case, we say $\boldsymbol{\lambda} = (\lambda_1, \lambda_2)$ is *resonant* of order r. This is known as a *small divisors* problem.

The following theorem [2] states that we we can repeat this process for all orders $r \geq 2$ and eliminate all non-resonant terms from equation (1.10).

Theorem 1.2.1 (Normal Form Theorem)**.** *F can be reduced by polynomial transformation to the form*

$$J\mathbf{y} + \sum_{r=2}^{N} w_r(\mathbf{y}) + O(|\mathbf{y}|^{N+1}), \tag{1.18}$$

where J is the Jordan form of $DF(\mathbf{0})$ and $w_r \in H^r$ is resonant of order r.

F is said to be in *normal form* if it is expressed as in (1.18). Alternatively, we say F is in normal form if it commutes with its linear term $DF(\mathbf{0})$. Note that, since F is an APM, preservation of area gives us

$$\lambda_1\lambda_2 = 1 \implies \lambda_1 = 1/\lambda_2, \tag{1.19}$$

and plugging (1.19) in equation (1.17), we get the resonant conditions

$$m_1 = m_2 + 1 \qquad \text{if} \qquad m_1 > m_2, \tag{1.20}$$

$$m_2 = m_1 + 1 \qquad \text{if} \qquad m_2 > m_1. \tag{1.21}$$

The resonant terms in the first (resp. second) component of F are associated with (1.20) (resp. (1.21)). These terms appear for all orders $r \geq 2$ and are called *inevitable* resonant terms. The reason for this nomenclature will be explained later.

The BNF for an APM F having a hyperbolic fixed point at $\mathbf{0}$ only has the linear term and the inevitable resonances up to any order because small divisors do not appear in this case.

1.2.1 Birkhoff Normal Form and twist maps

Now consider $p = \mathbf{0}$ to be an elliptic fixed point with multiplier $\lambda = e^{2\pi i\alpha_0}$. If we perform the change of variables to *Poincaré action-angle variables*, defined by

$$(x, y) = (2\tau)^{1/2}(\cos\theta, \sin\theta), \tag{1.22}$$

to expression (1.18), and assuming λ is not a root of unity of degree s or less, we obtain

$$(\theta_1, \tau_1) = (\theta + \alpha_0 + \sum_{i=1}^{M} \alpha_i\tau^i + R_\theta(\theta, \tau), \tau + R_\tau(\theta, \tau)), \qquad M = [s/2] - 1, \tag{1.23}$$

where R_θ, R_τ are $o(\tau^M)$. Note that, since θ is an angular coordinate, it is computed mod 1. We then say F is in *Birkhoff Normal Form (BNF)*. The expression

$$(\theta_1, \tau_1) - (R_\theta(\theta, \tau), R_\tau(\theta, \tau)) = (\theta + \sum_{i=0}^{M} \alpha_i \tau^i, \tau) \tag{1.24}$$

is known as the *(truncated) BNF* to order s, and it is denoted by BNF_s.

When α_0 is irrational, M may be taken to be arbitrarily large, thus removing the residual dependence on θ appearing in R_θ, R_τ to arbitrarily high orders of τ. The only resonant terms present in this case are the ones in (1.20) and (1.21). They are *inevitable* because they occur for all values of α.

On the other hand, if $\alpha_0 = p/q$, then *additional* resonances show up. In Poincaré variables, these resonant terms are not functions of τ alone, so the map cannot be reduced to the form $(\theta + \alpha(\tau), \tau)$ to arbitrarily high order in τ anymore. The requirement that λ is not a root of unity of degree s or less prevents these resonant terms from occuring at any order lesser than or equal to s. These additional resonances are also known as *evitable* resonances, since with a small change of the parameter α they do not longer appear. In particular, when λ is a root of unity of degrees 2,3 or 4 we talk about *strong resonances*. These cases are special because the resonant terms are of the same order as the lowest order terms in (1.23), and the elliptic point need not to be stable anymore. The study of these resonances are not within the scope of this work. For further information, please refer to [27].

Elliptic points with a multiplier λ that is not a root of unity of degree $s \geq 5$ are said to be *generic* if $\alpha_1 \neq 0$. This condition is sufficient for the BNF_s (1.24) to be an (integrable, see definition 1.2.3 below) area-preserving *twist map* [18].

Definition 1.2.1. A diffeomorphism T of the annulus $\mathbb{S}^1 \times (-1, 1)$ (or, equivalently, the cylinder) is said to be a *twist map* if

1. T preserves orientation.
2. T preserves boundary components, that is, there exists $\epsilon > 0$ such that if $(x, y) \in \mathbb{S}^1 \times (-1, -1 + \epsilon)$, then $T(x, y) \in \mathbb{S}^1 \times (-1, 0)$.
3. $\frac{\partial}{\partial y} \hat{T}_1(x, y) \neq 0 \ \forall (x, y) \in \mathbb{R} \times (0, 1)$, where $\hat{T} = (\hat{T}_1, \hat{T}_2)$ is a *lift* of T, that is, a map $\hat{T} : \mathbb{R} \times (-1, 1) \to \mathbb{R} \times (-1, 1)$ such that $\pi \circ \hat{T} = T \circ \pi$, where $\pi : x \mapsto x \pmod 1$ is the projection from $\mathbb{R}$ to $\mathbb{S}^1$. Since a lift is unique up to an additive integer [2], once a lift is chosen, all computations should use the same lift.

In action-angle coordinates, an area-preserving twist map is written as

$$T : (\theta, \tau) \mapsto (\theta + \alpha(\tau), \tau). \tag{1.25}$$

For a given $\tau \in (-1,1)$, $\alpha(\tau)$ is known as the *rotation number* of the orbit, defined for homeomorphisms of the circle [2] as follows.

Definition 1.2.2. Let $f : \mathbb{S}^1 \to \mathbb{S}^1$ be a homeomorphism of the circle and $\hat{f} : \mathbb{R} \to \mathbb{R}$ a lift of f. The *rotation number* of f is the limit

$$\rho(\hat{f}) := \lim_{n\to\infty} \frac{\hat{f}^n(x) - x}{n}. \tag{1.26}$$

Remark. ρ exists for all $x \in \mathbb{R}$, is independent of x and well defined up to an integer. Moreover, the limit does not depend on the lift chosen, so $\rho = \rho(f) = \rho(\hat{f}) (\mathrm{mod}\ 1)$ is well-defined.

Applying expression (1.26) to T, it is easy to see that $\alpha(\tau)$ is the rotation number of the orbit of T with radial coordinate τ.

Let us explain how the previous concept is adapted to the setting of APMs. For an arbitrary APM $F : \mathbb{R}^2 \to \mathbb{R}^2$, $F = (F_1, F_2)$, we shall restrict ourselves to an annulus $A = \mathbb{S}^1 \times (a,b)$ and consider a lift $\hat{F} = (\hat{F}_1, \hat{F}_2) : \mathbb{R} \times (a,b) \to \mathbb{R} \times (a,b)$. For invariant curves, F can be restricted to the curve, and the limit is computed as in (1.26). As for periodic points, the limit is defined using $\hat{F}_1$ in (1.26). For other points, such as points belonging to islands of figure 1.1, the limit is also defined and is the same as the periodic point inside the island. Nevertheless, there are other points for which limit (1.26) might not be defined, such as most of the points in bounded chaotic regions.

The dynamics of T is now clear: Orbits lie on circles of radius $\tau = \tau_0$ surrounding the origin (equivalently, at τ_0 in the vertical direction of the cylinder), and behave like a rotation of angle $\alpha(\tau_0)$, which is the rotation number of the orbit. Therefore, it differs from a linear rotation in that the rotation number changes with τ. In fact, in Poincaré variables, condition 3 from definition 1.2.1, known as the *twist condition*, translates to

$$\frac{d\alpha}{d\tau}(\tau) \neq 0, \qquad \tau \in (-1,1). \tag{1.27}$$

Then, α is a continuous monotone function of τ. Hence, it takes values on the *twist interval* $(\alpha(-1), \alpha(1)) = (\alpha_-, \alpha_+)$, and there is a one to one correspondence between the set of orbits and the twist interval, which allows us to tag each orbit with its own unique rotation number. That is, the so-called *frequency map* [1] is a one-to-one correspondence between the action space and the frequency space.

When $\alpha(\tau_0)/2\pi = p/q \in \mathbb{Q}$, where $p, q \in \mathbb{Z}$, $q \neq 0$ and $\gcd(p,q) = 1$, we have

$$T^q(\theta_0, \tau_0) = (\theta_0 + q \cdot 2\pi p/q, \tau_0) = (\theta_0, \tau_0), \tag{1.28}$$

and (θ_0, τ_0) is a periodic point of period q. On the other hand, if $\alpha(\tau_0)/2\pi \in \mathbb{R}\backslash\mathbb{Q}$, then

$$T^m(\theta_0, \tau_0) = (\theta_0 + 2m\pi\alpha(\tau_0), \tau_0) \neq (\theta_0, \tau_0) \tag{1.29}$$

and there are no periodic points: The orbit of any point with $\tau = \tau_0$ fills the circle densely, and T has an invariant curve at $\tau = \tau_0$. If T is defined on the cylinder, the curve is said to be a *rotational* invariant curve (r.i.c.). As an example of *integrable* area-preserving twist map, we will use Chirikov's standard map (4) with $k = 0$.

Definition 1.2.3. An APM $F : U \to \mathbb{R}^2$, $U \subset \mathbb{R}^2$ is said to be *(analytically) integrable* if there exists an (analytic) non-constant function $G : U \to \mathbb{R}$ such that $G(x) = G(F(x))\ \forall x \in U$.

Remark. For an integrable twist map (1.25), the action τ plays the role of G above.

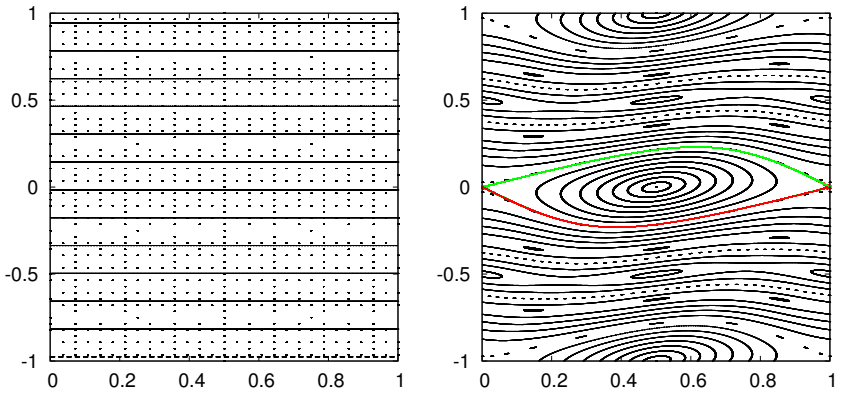

Figure 1.4: **Left:** Phase space of S_k for $k = 0$. **Right:** Phase space of S_k for $k = 0.5$.

The phase space of (4) for $k = 0$ is depicted on the left of figure 1.4. We observe that, for $y \in \mathbb{Q}$, the standard map has a periodic orbit (in particular, all points with $y = 0$ are fixed points), whereas if $y \in \mathbb{R}\backslash\mathbb{Q}$, the mapping presents an invariant curve, in concordance with the discussion of twist maps presented above.

On the other hand, if $k > 0$, the integrability condition is lost. The map has an elliptic fixed point at $(1/2, 0)$ and a hyperbolic fixed point at the origin. Moreover, (4) is reversible with respect to the axis $x = 1/2$ for all values of k, and is 2π-periodic in both x and y. Therefore, it can be defined on the torus $\mathbb{S}^1 \times \mathbb{S}^1$. From this periodicity, we infer that the mapping has an elliptic fixed point for $(1/2, m)$ and a hyperbolic fixed point at $(0, m)\ \forall m \in \mathbb{Z}$, $\forall k > 0$.

These hyperbolic points present the same dynamics as the Hénon map, which include validity of theorem 1.1.1, and the presence of stable and unstable manifolds, as can be seen on the right of figure 1.4.

1.2.2 The Moser Twist Theorem

Focusing on the same figure, we observe that invariant curves from the left of figure 1.4 are now deformed after increasing the value of k, and elliptic points in periodic orbits have invariant curves surrounding each point of the orbit. This happens in the same fashion as in (3): As we observed in figure 1.1, there are invariant curves surrounding the origin, as well as a 5-periodic orbit of elliptic points which also has curves surrounding each of its points.

We now ask ourselves if an invariant curve with rotation number $\alpha \in \mathbb{R}\backslash\mathbb{Q}$ will survive under small parameter changes. For this purpose, let

$$T_\epsilon(\theta,\tau) = T(\theta,\tau) + P(\theta,\tau,\epsilon) \tag{1.30}$$

be a perturbation of (1.25), where

$$\begin{aligned} P : \mathbb{S}^1 \times (-1,1) &\to \mathbb{R}^2 \\ (\theta,\tau) &\mapsto (f(\theta,\tau,\epsilon), g(\theta,\tau,\epsilon)) \end{aligned} \tag{1.31}$$

is a 2π-periodic in θ analytic (real) function, and $P(\theta,\tau,0) \equiv \mathbf{0}$. Furthermore, we will suppose T_ϵ is area-preserving for all values of ϵ. Note that, for $k > 0$, (4) satisfies these conditions with $\epsilon = \frac{k}{2\pi}$, $P(\theta,\tau,k) = (\frac{k}{2\pi}\sin(2\pi\theta), \frac{k}{2\pi}\sin(2\pi\theta))$.

The following theorem [21] guarantees, under certain assumptions, that an invariant curve of T will survive for T_ϵ.

Theorem 1.2.2 (Moser Twist)**.** *Given any irrational number $\omega \in (\alpha_-, \alpha_+)$ satisfying*

$$\left|\frac{\omega}{2\pi} - \frac{p}{q}\right| > \frac{C}{q^\tau} \qquad \forall p,q \in \mathbb{Z},\ q \neq 0 \tag{1.32}$$

for a given $C > 0$ and $\tau \geq 2$, there exists a differentiable closed curve

$$\theta = \xi + G(\xi,\epsilon), \qquad \tau = F(\xi,\epsilon), \tag{1.33}$$

with F, G analytic and 2π-periodic in ξ, which is invariant under the mapping T_ϵ, provided $|\epsilon|$ is sufficiently small. The image of a point in (1.33) *is obtained by replacing ξ by $\xi + \omega$.*

A real number ω satisfying (1.32) is said to be *diophantine*, or, equivalently, we say ω satisfies a $(C,\tau)-$*diophantine condition*. It is a measure of how well an irrational number can be approximated by rational numbers. If we use a *continuous fraction representation* [18] $\omega = [a_0; a_1, a_2, \dots]$ with $a_i \in \mathbb{Z}$, which corresponds to

$$\omega = a_0 + \cfrac{1}{a_1 + \frac{1}{a_2 + \dots}}, \tag{1.34}$$

w will have a better diophantine condition the sooner we have an infinite sequence of ones, denoted by 1^∞. In this case, we will say w is a *noble irrational number*. In particular, the *golden ratio*

$$\varphi = \frac{\sqrt{5}-1}{2} \tag{1.35}$$

is the "noblest number", since it is diophantine for $\tau = 2$. Its continuous fraction representation is $\varphi = [0; 1^\infty]$.

Therefore, three factors come into play for the persistence of an invariant curve of a twist map under perturbation: The twist condition, ω and $|\epsilon|$. The larger the twist condition or the better the diophantine condition is, the larger perturbation $|\epsilon|$ is allowed.

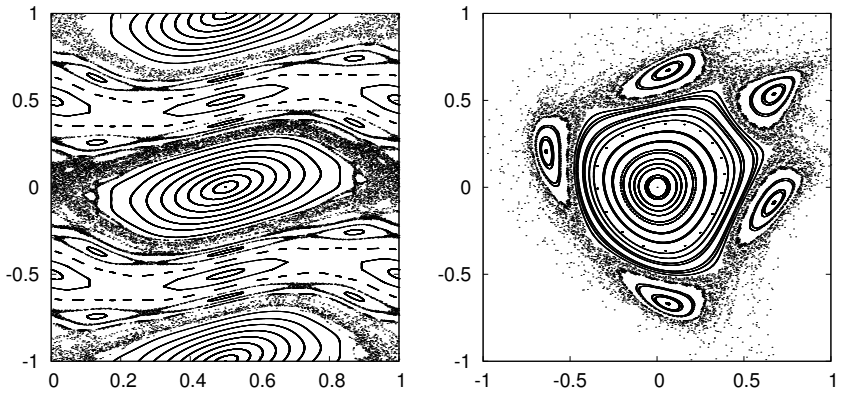

Figure 1.5: **Left:** Phase space of S_k for $k = 0.98 > k_G$. **Right:** Phase space of the Hénon map for $a = 0.215$.

When changing the parameter a in (3) or k in (4), the size of the parameter also changes, and we expect some invariant curves to persist and some others to break down. The ones with the most diophantine rotation number will survive for larger increments of the parameter, whereas the curves with the least diophantine rotation numbers will disappear with small increments.

For the standard map, the last rotational invariant curve has rotation number equal to the golden ratio (1.35) and breaks down at the *Greene parameter* [11]

$$k_G \simeq 0.971636\ldots \tag{1.36}$$

Invariant curves are very important for the dynamics of APMs. Indeed, orbits cannot cross invariant curves, since it would contradict the preservation of orientation. Consequently, the motions in a region between two invariant curves are trapped in what is known as a *Birkhoff instability zone* [27]. In particular, chaotic

motions are trapped in this instability zone. This can be observed in figure 1.1 and on the left of figure 1.4.

As a consequence, the breakdown of invariant curves allows *diffusion*, that is, it allows previously trapped motions to be able to navigate the phase space freely. Just after the the last invariant curve has disappeared, the diffusion is very slow because it requires a lot of iterates for an orbit to reach a previously unreachable part of the phase space. This is because a small decrease in parameter would make this invariant curve to reappear.

In figure 1.5 we can see how the destruction of invariant curves affects the dynamics of APMs: On the left, the phase space of the standard map is depicted for a value of k greater than k_G. This means all the r.i.c.'s are already broken down, and points can navigate the cylinder freely. However, a large number of periodic orbits remain, and it takes a lot of iterates for a point to cross them, since they tend to get near the invariant curves surrounding the points in the orbit and follow their periodic motion, which is horizontal. Most of these periodic orbits, which form some sort of island chains, were already present on the right of figure 1.4. With the increase of the parameter, however, some of them have disappeared, whereas some others seem to have gotten bigger in size, in the sense that the invariant curves of every island now enclose a bigger region.

On the other hand, the phase space of the Hénon map is depicted on the right of figure 1.5 for the value $a = 0.215$. The invariant curves surrounding the five islands have been broken down by the change of the parameter, and thus, the chaotic motions, which were previously trapped between this destroyed invariant curve and the remaining outermost one, can now move freely.

Nevertheless, it seems that the five islands from figure 1.1 are still present on the right of figure 1.5, despite the increase of parameter, which is large enough to break down the invariant curves that were surrounding these islands.

1.2.3 The Poincaré-Birkhoff theorem

The main aim of this section is to understand the nature of the islands seen in figures 1.1, 1.4 (right) and 1.5 (right), how they affect the dynamics of an APM and their persistence under perturbation. As we have commented before, even though the changes in the parameter for the aforementioned figures is enough to break down some invariant curves (all in the case of the standard map), there are some periodic orbits that persist, and they change in size with a parameter change. Additionally, these orbits might somehow affect the chaoticity of orbits around them.

Recall that, for $\alpha/2\pi = p/q \in \mathbb{Q}$, the twist map (1.25) has a periodic orbit of period q. Next theorem [2] ensures the survival of this orbit under perturbation.

Theorem 1.2.3 (Poincaré-Birkhoff). *Given any rational p/q between $\alpha_-/2\pi$ and $\alpha_+/2\pi$, there are $2q$ fixed points of T_ϵ^q satisfying*

$$T_\epsilon^q : (\theta, \tau) \mapsto (\theta_q, \tau_q) = (\theta + 2\pi p, \tau) \tag{1.37}$$

provided that $|\epsilon|$ is sufficiently small.

These $2q$ fixed points of T_ϵ^q are $q-$periodic points of T_ϵ. In particular, these are arranged in two q-periodic orbits, one comprised of q elliptic points (the points at the center of the islands) and another one of hyperbolic points (each located between any two consecutive islands). This can be checked by computing the eigenvalues of DT^q evaluated at each periodic point.

Note that, by perturbing T, additional resonances appear in its normal form. These resonances show up on the phase space in the form of islands, which is why both terms are used indistinctively. Indeed, we know that if the elliptic point is generic, the truncated BNF is a twist map. Since the actual mapping has these islands whilst the truncated BNF does not (because it is a twist map), then the islands must appear because of the difference between the BNF and the truncated BNF, i.e. (R_θ, R_τ). Then, to see resonances of order $m \geq 5$, one needs to consider $\alpha = \frac{q}{m} + \delta$, $1 \leq q < m$, $\gcd(q, m) = 1$, where $\lambda = e^{2\pi i \alpha}$ is the multiplier of the elliptic fixed point. In this case, the island chain is called the $q : m$ resonance.

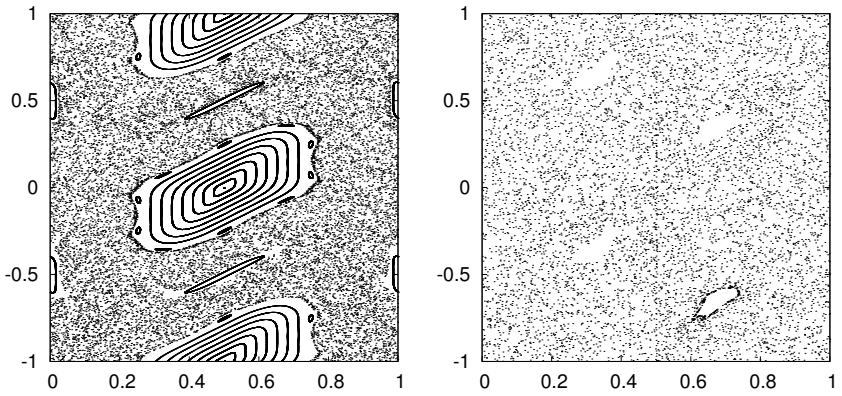

Figure 1.6: **Left:** Phase space of S_k for $k = 2$. **Right:** Phase space of S_k for $k = 5$. See the text for more information.

Focusing on the $q : m$ resonance and considering T_ϵ^m as the main mapping, each elliptic point will have a multiplier λ_m, and we can apply theorems 1.2.2 and 1.2.3 around an elliptic periodic point, which will be surrounded by invariant curves and islands in the same fashion as the origin for the Hénon map. Moreover, all these invariant curves and satellite islands jump from one island to the next one

in the main resonance. Therefore, the whole mapping repeats on a smaller scale, creating a *island-around-island fractal* structure. As for the hyperbolic points, we have already commented that they have invariant stable and unstable manifolds and that theorem 1.1.1 applies when considering the convenient power of the mapping. Moreover, the increase of the parameter will destroy these resonances, which will lead to a bigger chaotic region. This is depicted in figure 1.6, where we have plotted the standard map for the values $k = 2$ (left) and $k = 5$ (right). In the former, there are still invariant curves surrounding the elliptic point at $(1/2, 0)$, and the 1:2 resonance has not been destroyed yet. In the latter, all resonances visible in the former are destroyed, and the cylinder appears chaotic. Note that there are always resonances (of higher periods) even if we cannot see them due to numerical precision. In fact, it is an open question [3, 16] if there is any open subset of the domain of an APM where there are no islands.

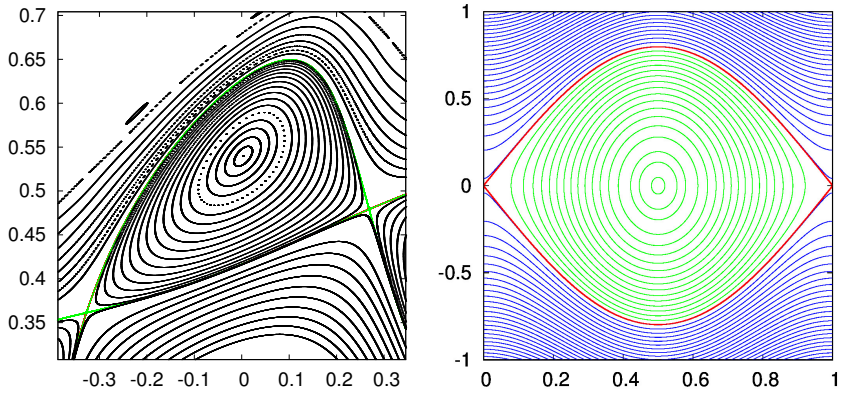

Figure 1.7: **Left:** Close-up of the phase space of H_α, $\alpha = 0.21$, around one of the islands of the 1:5 resonance. **Right:** Phase portrait (level curves of the Hamiltonian) of the mathematical pendulum.

Notice that the phase space of an APM around an elliptic point of a resonance resembles the phase portrait of the mathematical pendulum, an integrable Hamiltonian system defined on the cylinder $\mathbb{S}^1 \times \mathbb{R}$, with Hamiltonian

$$H(x, y) = \frac{y^2}{2} + \frac{1}{2\pi}\cos(2\pi x), \tag{1.38}$$

and described by the ODEs

$$\dot{x} = y, \qquad \dot{y} = \sin(2\pi x). \tag{1.39}$$

This system has a saddle-type hyperbolic fixed point (unstable equilibrium) on the origin and one elliptic fixed point (stable equilibrium) at $(1/2, 0)$. The invariant

manifolds of the saddle (depicted in red) are *separatrices*, because they separate two regimes of motion: The orbits in-between the separatrices and around the elliptic point ($-1/2\pi < H < 1/2\pi$) correspond to *librational* motions (plotted in green), whilst the orbits of higher energy ($H > 1/2\pi$) are outside the region enclosed the separatrices, and correspond to *rotational* motions (plotted in blue). [18]

The similarities between the dynamics of an APM around an elliptic point of a resonance and the pendulum can be observed in figure 1.7, where a close-up of one island of the 1:5 resonance has been plotted (left), along with the phase space of the pendulum (right). Nevertheless, there are some notable differences:

- In the Hénon map, the invariant manifolds are not coincident. These transversal intersections form heteroclinic tangles, which create chaos. On the other hand, the pendulum is an integrable system, and the first integral (1.38) prevents from having transversal intersections between invariant manifolds. Thus, there can be no chaos in an integrable system.
- The Hénon map has infinitely many resonant islands, whereas this is impossible for an integrable system.
- The separatrices of the classical pendulum are symmetrical with respect to the axis $y = 0$. In contrast, the invariant manifolds surrounding an island in the Hénon map are not: The outer manifolds have more length than the inner ones, and the island looks more deformed than the region delimited by the separatrices of the pendulum[3].

Even though the invariant manifolds on the left of figure 1.7 seem coincident, we know they they intersect transversally[4]. This can be seen on the right of figure 1.8, where now the splittings of the invariant manifolds of the hyperbolic point at (-0.32748,0.36126) are evident. There are theoretical results, e.g. [10], showing that these splittings behave exponentially small in the parameter $\alpha - 0.2$ when $\alpha \to 0.2$ due to analyticity of the APM (see comments in the Introduction).

Now we can understand how important is (R_θ, R_τ) in equation (1.23): The truncated BNF is an integrable twist map, and does not have resonances nor chaos. When we encounter the first additional resonance, a resonance strip appears in the mapping. Now consider the normal form to any order plus additional resonant terms. The difference between the normal form and the mapping is (R_θ, R_τ), and it includes the splitting of the invariant manifolds. Since we can do the normal form procedure to any order, (R_θ, R_τ) must be exponentially small in the distance-to-bifurcation parameter, and splitting is a *beyond all orders* phenomenon (i.e. it does not appear on the normal form to any order considered) which is exponentially small in the aforementioned parameter.

[3] In fact, this is generic for any twist APM around an elliptic fixed point.

[4] This is true for the Hénon map, since it is an entire function

1.3 Homoclinic tangles: Horseshoes and topological chaos

As we have mentioned, the orbits of points near the invariant manifolds are chaotic. Indeed, on the left of figure 1.8, 10^6 points belonging to the orbit of the point $(-0.33500, 0.36300)$ are plotted in blue. The iterates of this point travel along the invariant manifolds of all the hyperbolic points in the periodic orbit. In addition, the iterates fill the region comprised between the invariant manifolds and the invariant curve surrounding the resonance strip, as observed on the right of figure 1.8.

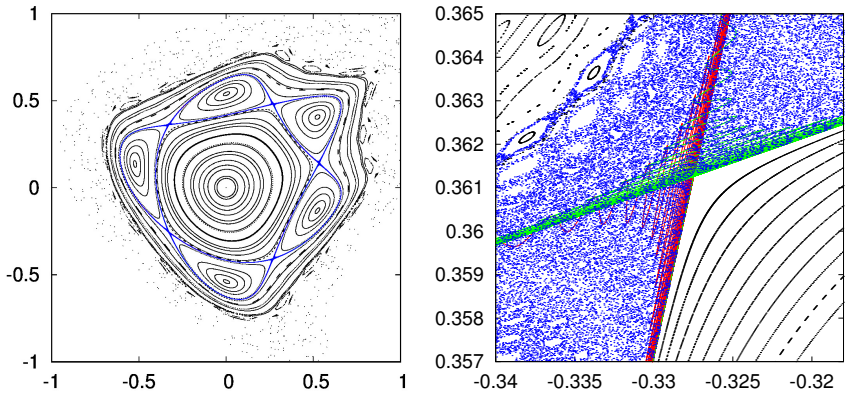

Figure 1.8: **Left:** Phase space of H_α, $\alpha = 0.21$ with the orbit of $(-0.33500, 0.36300)$ depicted in blue **Right:** Close-up of the figure on the left around the hyperbolic periodic point

The aim of this section is to understand what is needed to create chaos, and the mechanism through which it is created. There are three main ingredients which are necessary for the presence of chaos:

1. Hyperbolicity, given by the hyperbolic fixed point. Indeed, if there is stability (e.g. around an elliptic fixed point), there cannot be chaos, since orbits remain near the fixed point.
2. Transversality of the intersection of invariant manifolds. In fact, this is the most fundamental ingredient, since an integrable system might present hyperbolicity but there cannot be chaos (e.g. the pendulum).
3. Reinjection of the dynamics: This is guaranteed because of the accumulation of the invariant manifolds by lemma 1.1.3, which after a suitable number of iterates return to the starting point (see the left of figure 1.1: The lobes stretch after iterating the mapping, and eventually return near the first lobe). This reinjection allows more transversal intersections to happen and chaotic orbits to return nearby the hyperbolic point.

The question now is: How do transversal intersections of the invariant manifolds create chaos? To this end, we present the *horseshoe map* [25]. To define this mapping $f : \mathbb{R}^2 \to \mathbb{R}^2$, we employ the following procedure:

1. Take a square Q on the plane.
2. We contract Q in the horizontal direction and expand it on the vertical one.
3. We fold Q in the middle, forming the shape of a horseshoe.
4. We place the horseshoe so that it intersects the original square along two vertical strips.

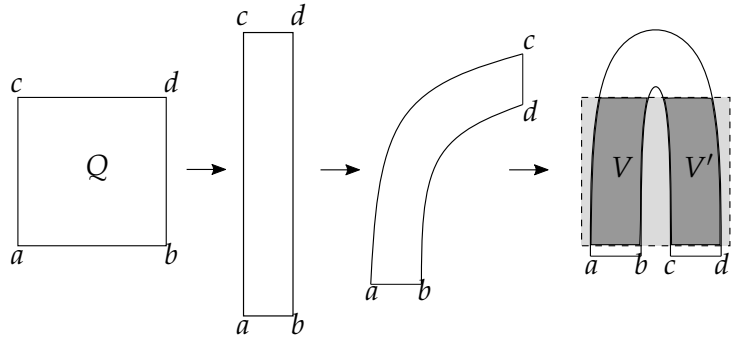

Figure 1.9: Construction of the horseshoe map. Steps 1 to 4 are depicted from left to right.

From figure 1.9 it is clear that $Q \cap f(Q) = V \cup V'$. This mapping is invertible, and the inverse map creates a horizontal horseshoe, so that after, unfolding the horseshoe, expanding the rectangle in the horizontal direction and contracting it in the vertical direction, we recover the original square. In this case, the horizontal horseshoe intersects Q in two horizontal strips.

Most of the points leave Q under iterates of f or f^{-1}. We are interested in those points that remain in Q, that is, the invariant set

$$\Lambda := \{x \in Q \mid f^k(x) \in Q \quad \forall k \in \mathbb{Z}\}. \tag{1.40}$$

If we iterate f twice, $Q \cap f(Q) \cap f^2(Q)$ is made of four vertical strips, and if we do it for f^{-1}, we obtain four horizontal strips. In general, the intersection $\cap_{k=0}^{n} f^k(Q)$, $n \geq 0$, is made up of 2^n vertical strips, and the same number of horizontal strips is obtained if we consider f^{-1}. We then want to consider the set

$$\bigcap_{k=-n}^{n} f^k(Q) \supset \Lambda. \tag{1.41}$$

which is depicted in figure 1.10 for $n = 2$. This set has a very complicated structure, and it is in fact a hyperbolic *Cantor set* with zero measure [17].

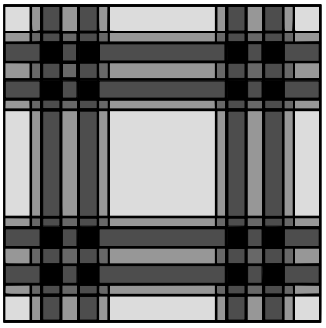

Figure 1.10: Intersection of Q and its two first images under f and f^{-1}.

Now consider the set

$$\mathcal{A}_2^{\mathbb{Z}} := \{s = \ldots s_{-1}s_0s_1s_2\ldots,\ s_i \in \{0,1\}\} \tag{1.42}$$

and the *shift map* $\sigma : \mathcal{A}_2^{\mathbb{Z}} \to \mathcal{A}_2^{\mathbb{Z}}$ defined by

$$\sigma(s) = s' \qquad \text{if} \qquad s'_j = s_{j-1} \quad \forall j \in \mathbb{Z}. \tag{1.43}$$

Theorem 1.3.1. *There is a one-to-one map correspondence*

$$\begin{aligned} h : \Lambda &\to \mathcal{A}_2^{\mathbb{Z}} \\ x &\mapsto s \end{aligned} \tag{1.44}$$

Moreover,

$$h(f(x)) = \sigma(h(x)) \tag{1.45}$$

Theorem 1.3.1 tells us that the dynamical systems (Λ, f) and $(\mathcal{A}_2^{\mathbb{Z}}, \sigma)$ are topologically conjugated, see (1.7). The next theorem [25] tells us that the latter has chaotic dynamics, and therefore, so does the former.

Theorem 1.3.2. *The horseshoe map has a closed invariant set Λ that contains:*

1. *A countable set of periodic orbits of arbitrarily long period.*
2. *An uncountable set of non-periodic orbits.*
3. *Dense orbits.*

These three type of orbits are enough to guarantee the presence of chaos. As a consequence, we might pick any two points in Λ which have the same sequence in $\mathcal{A}_2^{\mathbb{Z}}$ up until some point, which means that they are arbitrarily close (with a suitable distance [17]), and see how after a number of iterates they end up arbitrarily far. This is known as *sensitivity to initial conditions*, and it is a property of chaos.

But why is the horseshoe map so important? The following result states that any APM having a hyperbolic fixed point with a transverse homoclinic point has a horseshoe as a subsystem.

Theorem 1.3.3 (Birkhoff-Smale). *Let $F : U \in \mathbb{R}^2 \to \mathbb{R}^2$ be an APM with a hyperbolic fixed point at the origin* **0** *which has a transverse homoclinic point p. Then in an arbitrarily small neighbourhood of* **0** *there exists a horseshoe for some iterate of F.*

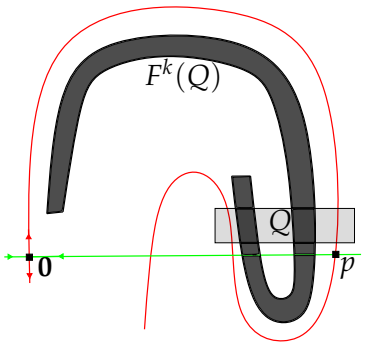

Figure 1.11: Sketch of the horseshoe in an APM with a transverse homoclinic point in a neighbourhood of a hyperbolic fixed point.

Therefore, APMs have a horseshoe (in fact, an infinite number of them) and, as a consequence, chaos. However, this chaos affects a set of points of zero measure in the phase space of F (because Λ has zero measure), which means that it might not be observed when studying the dynamics of F. Nevertheless, every hyperbolic point in an APM has invariant manifolds with an infinite number of transversal homoclinic and heteroclinic points.

In fact, the invariant manifolds of one hyperbolic point do not only intersect with the invariant manifolds of the other points in the periodic orbit, but with the invariant manifolds of hyperbolic points of other periods, creating infinitely many homoclinic and heteroclinic tangles. This, together with the fact that an invariant curve traps the chaotic motion, helps the chaos to seemingly have positive measure, and therefore to be visible. Note that the positive measure is apparent (in the sense that chaos is visible), however we can not assure that: As we have said before, it is an open problem known as the *positive entropy conjecture* [3, 16].

For details and proofs on the topic, we refer to [12, 17, 25, 28].

Chapter 2

Numerical exploration of the weakly-dissipative regime

In many situations, conservative dynamical systems model an idealization of real-life processes but non-conservative forces, such as friction or medium resistance, play an important role in the evolution in time of the system, and must be considered to obtain a more accurate description of the process. For instance, the classical pendulum, with Hamiltonian (1.38), describes the motion of a pendulum without friction. A more accurate description of the motion of a pendulum involves the perturbation of this model introducing dissipative forces.

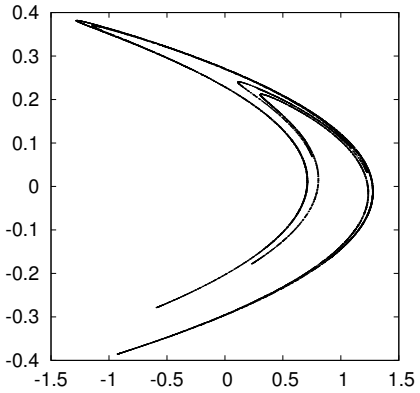

Figure 2.1: Strange attractor of the classical dissipative Hénon map.

Throughout this chapter, we will study how dissipation affects the dynamics of APMs. Specifically, we study a dissipative perturbation on a uniparametric family of analytic APMs $\{F_\alpha : U \subset \mathbb{R}^2 \to \mathbb{R}^2\}_{\alpha\in\mathbb{R}}$. The perturbation will be different depending on the family considered: For the Hénon map, the dissipation

considered in (5) is radial. It is related to the classical dissipative Hénon map [15]

$$H_{a,b} : \begin{pmatrix} u \\ v \end{pmatrix} \mapsto \begin{pmatrix} 1 - au^2 + v \\ bu \end{pmatrix} \tag{2.1}$$

by introducing parameters $b = (1-\epsilon)^2$ and $a = b(\cos^2(2\pi\alpha) - 2\cos(2\pi\alpha))$. This version of the dissipative Hénon map is of interest because of the existence of a strange attractor (see figure 2.1) for the values $a = 1.4$, $b = 0.3$ [15]. Note that the definition of a and b defines a one-to-one correspondence between $(\alpha, \epsilon) \in [0, 1/2] \times [0, 1]$ and $(a, b) \in [-b, 3b] \times [0, 1]$, hence the classical values are not included in the domain (ϵ is, but α becomes complex). We are interested in the study of weak dissipation ($\epsilon \ll 1$), that is, close to the conservative case. On the other hand, the dissipation applied on (6) points towards $y = 0$. In both cases,

$$\det DF(x, y) = 1 - \epsilon < 1 \quad \forall (x, y) \in U, \tag{2.2}$$

where F is either the dissipative Hénon map or the dissipative standard map, and U is the corresponding phase space. A diffeomorphism $F : U \to \mathbb{R}^2$ satisfying (2.2) is said to be *dissipative* with constant jacobian.

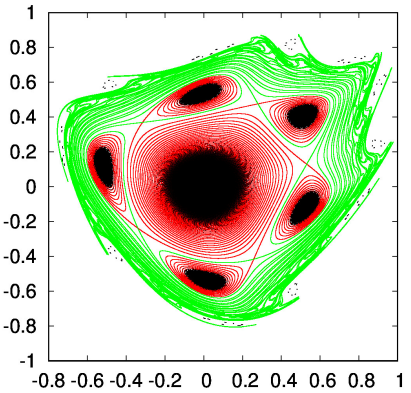

Figure 2.2: Phase space of the dissipative Hénon map for $\alpha = 0.21$ and $\epsilon = 10^{-3}$. The 1:5 resonance persists under this dissipation, and the stable and unstable invariant manifolds of the saddles are depicted in green and red, respectively. Additionally, we see that a resonance of period 11 has survived as well.

Note that, despite restricting ourselves to two types of dissipation, the phenomena showed are rich and varied. In fact, if the dissipation depends on (x, y) smootly, most of the arguments used in this chapter can be adapted [23].

The evolution of the conservative case to the dissipative scenario is driven by the destruction of topological structures present in the former. In particular, no

invariant curves can survive on $\mathbb{R}^2$ under radial dissipation. Indeed, suppose there were one such curve, then F would have to preserve the area enclosed by it, A, i.e. $F(A) = A$. However, this contradicts the fact that F is dissipative, since

$$\text{Area } (F(A)) = (1-\epsilon)\text{Area } (A) < \text{Area } (A) \tag{2.3}$$

for any enclosed region A. On the cylinder, at most one r.i.c. can persist under dissipation [2] since it does not enclose an area. These statements can be checked in figure 2.2. If we consider two r.i.c.'s on the cylinder, they would also enclose an area on this surface, and we would be in the same situation as in (2.3).

On the other hand, depending on the size of dissipation, Birkhoff periodic orbits can persist under sufficiently small dissipative perturbations [2]. Indeed, assume $x_* \in U$ is a q-periodic point of F belonging to such an orbit, and consider the mapping

$$G(x, \epsilon) = ((1-\epsilon)F(x))^q - x, \qquad x \in U. \tag{2.4}$$

Clearly, $G(x_*, 0) = \mathbf{0}$, and the Implicit Function Theorem guarantees the existence of the q-periodic point for sufficiently small $\epsilon > 0$. Accordingly, in figure 2.2 we observe that the 1:5 resonance and a 11-periodic orbit of the conservative Hénon map have persisted under dissipation. In particular, fixed points will survive, although their cooordinates will depend on ϵ. For the dissipative Hénon map, the fixed point located at the origin in the conservative case persists for all values of ϵ, while the hyperbolic fixed point p_h (see section 1.1) is located at

$$p_h(\epsilon) = \left(\frac{1 - 2c\mu + \mu^2}{\mu s}, \frac{(\mu - c)(1 - 2c\mu + \mu^2)}{\mu s^2} \right), \tag{2.5}$$

where $c = \cos(2\pi\alpha)$, $s = \sin(2\pi\alpha)$ and $\mu = 1 - \epsilon$. On the other hand, for the standard map, the hyperbolic fixed point is located at

$$p'_h(\epsilon, \omega) = \left(\frac{1}{2\pi} \arcsin\left(\frac{\epsilon\omega}{K}\right), -\omega \right), \tag{2.6}$$

where $K = k/2\pi$. The elliptic fixed point that was at $(1/2, 0)$ for the conservative case is now located at $p'_h(\epsilon, \omega) + (1/2, 0)$.

Nevertheless, the type of these points has changed in the dissipative regime, as observed in figure 2.2. Indeed, perturbed elliptic points become *stable foci*, and they are no longer neutrally stable but assymptotically stable (in particular, they are linearly stable). These foci are *attractors*, invariant objects where the long-term dynamics of the system is concentrated. Furthermore, the invariant curves that were surrounding elliptic points have been replaced by *basins of attraction* of the foci [27], which are the regions of the phase space whose points are captured by the corresponding focus. This concept will be further discussed in section 2.2.

On the other hand, hyperbolic points persist since hyperbolicity is an open condition (see definition 1.1.3). In particular, they have their stable and unstable manifolds which evolve under dissipation, that is, a resonant structure will change its topology depending on the size of the dissipation [23]. According to the relative (to the size/order of the resonance) stress of the dissipation, we distinguish:

1. *Strong dissipative perturbation*: The resonance is destroyed in a saddle-focus bifurcation [23]: The saddle and the focus collide and disappear when increasing ϵ. This explains why in figure 2.2 only two resonances survive the dissipation: For other resonances (of higher order), the dissipation is strong enough relative to their size in phase space.
2. *Medium size dissipative perturbation*: The resonance persists but dissipation has destroyed all homo/heteroclinic points of the resonant structure (related to the invariant manifolds of saddles of the same period), becoming flow-type. This is the case of the 5-order resonance observed in figure 2.2. The topology of the resonances resembles the phase space of the pendulum under dissipation, justifying why we call them flow-type resonances. In this case, the invariant manifolds define an "entrance channel" to the periodic attractor and a "crossing channel" allowing points to pass through the resonant chain.
3. *Weak dissipative perturbation*: For a small dissipation, the resonance keeps the topological shape from the conservative case, with homo/heteroclinic points. As the dissipative parameter is increased, these are destroyed and the resonance becomes of flow type.

We are interested in a weak dissipative perturbation, since the most compelling aspect of introducing dissipation is to observe which structures survive from the conservative case. Nevertheless, note that all scenarios above coexist when considering a fixed ϵ and studying the dynamics of outlasting resonances at different distances from the perturbed elliptic point [23].

On the other hand, we note that there is chaos in the dissipative scenario when homo/heteroclinic points persist (indeed, the Birkhoff-Smale theorem 1.3.3 can be adapted to the dissipative setting). Nevertheless, it is not chaos in the conservative sense (as seen in section 1.3), but a temporary chaos: Every point ends up in an attractor (or infinity), since the long-term dynamics is concentrated there.

This chapter is organized as follows: First, we will study the evolution of the invariant manifolds of the saddles of dissipative APMs, emphasizing the fact that their topology is different depending on the map considered, their location on the phase space and the combination of parameters. Secondly, we will study the coexistence of attractors of the dissipative Hénon map for $\alpha = 0.21$, looking at the ratio of points captured by each attractor. Finally, we will do a numerical exploration

of the dissipative standard map, where the addition of a third parameter ω allows the system to have different types of attractors aside from the ones seen in the dissipative Hénon map.

2.1 Topology of stable and unstable manifolds of hyperbolic points

As mentioned previously, hyperbolic points persist under dissipation, and their invariant manifolds evolve as dissipation increases. The first noticeable trait is that the splitting, which was exponentially small in the conservative case, is no longer so. In fact, in the dissipative case the splitting of invariant manifolds is of order ϵ.

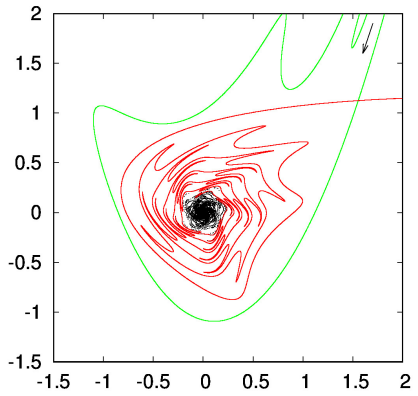

Figure 2.3: Phase space of the dissipative Hénon map for $\alpha = 0.21$ and $\epsilon = 0.05$. The stable and unstable manifolds of the saddle are plotted in green and red, respectively.

In figure 2.3 we can see the invariant manifolds of $p_h(\epsilon)$ of the Hénon map for $\alpha = 0.21$ and $\epsilon = 0.05$. In comparison with figure 1.1, we see that all the homoclinic points are destroyed, and the unstable manifold has a spiral shape with the origin as its center. All the points in the "entrance channel" (marked with an arrow in the plot) follow the spiral and tend to the focus at the origin. Moreover, it does not take much iterates to reach the origin. In fact, picking initial conditions along the curves of symmetry of the conservative case, iterating 2000 each and plotting from the 10th iterate, we obtain the black dots in figure 2.3, which are quite close to the focus. The rest of the points follow the stable manifold until they are close to the saddle, where, by theorem 1.1.1, will then follow the unstable manifold to infinity.

The situation displayed in figure 2.3 is such that all resonant structures (that evolve from the conservative case) are destroyed. It is clear that dissipation has destroyed all homoclinic points of the invariant manifolds of $p_h(\epsilon)$ in 2.3, and since there are no resonances outside the region enclosed by the invariant manifolds of the hyperbolic fixed point, then all resonances inside must be either destroyed or without any homo/heteroclinic points. We can conclude we are in the former scenario by the behaviour of points under iteration.

For the dissipative standard map, if we set $\omega = 0$ we have a focus at $(1/2, 0)$ and a hyperbolic fixed point at the origin. The invariant manifolds behave as in the dissipative Hénon map. However, in this case, points from above and below the focus are attracted by it, and hence we find two "channels" created by the invariant manifolds which direct all points towards the attractor. Moreover, in contrast with the invariant manifolds seen in 2.3, here we have that, even in the strong dissipative scenario, all long-term dynamics is concentrated in this focus, that is, points cannot escape to infinity as in the dissipative Hénon map.

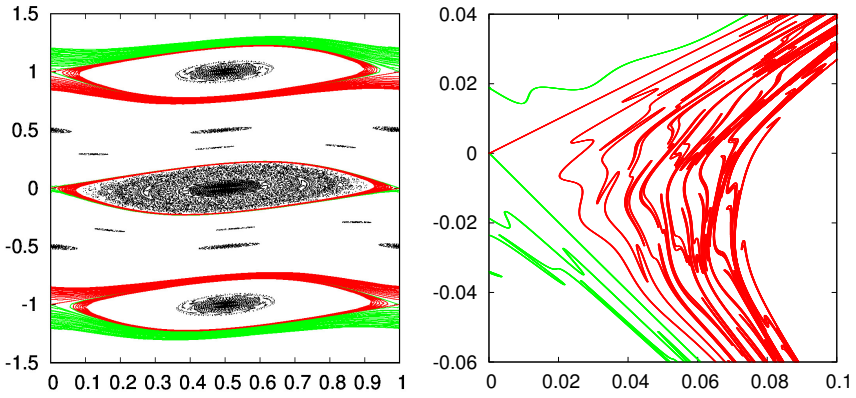

Figure 2.4: **Left:** Dissipative standard map for $k = 0.5$, $\epsilon = 10^{-3}$ and $\omega = 0$. The stable and unstable manifolds of the saddles are plotted in green and red, respectively. In addition, we can see the coexistence of attracting periodic orbits of periods 2 and 3. **Right:** Close-up around the hyperbolic fixed point at the origin.

The other elliptic fixed points of the mapping (6), located near $x = 1/2$ and $y \in \mathbb{Z} \setminus \{0\}$, also turn into foci under dissipation. Nevertheless, the topology of the invariant manifolds is different in this case: As for the resonant structures of the Hénon map, not all points are captured by these foci, and the invariant manifolds create two channels: One "entrance channel" through which points get to the attractor, and one "crossing channel" through which points can travel towards $y = 0$ until they are captured by another attractor.

See the left of figure 2.4, where the phase space of the dissipative standard map

for $k = 0.5$, $\epsilon = 10^{-3}$ and $\omega = 0$ is depicted, along with the invariant manifolds surrounding three perturbed elliptic fixed points. On the right of the same figure, a magnification around the saddle located at the origin is shown, confirming that all homoclinic points are destroyed. In addition, we see that the invariant manifolds fold in a strange manner: This is due to the fact that in between there are invariant manifolds belonging to other resonances as well, and they try not to intersect each other by folding. In fact, if we were to plot these other invariant manifolds, we would see they fold in the same manner as the ones depicted. Moreover, although in 2.3 there is a larger dissipation parameter, we can hold the same phenomenon accountable for the foldings seen there.

For a concrete resonance, the transition from the medium-dissipative to the weakly-dissipative scenario is related to the fact homoclinic and heteroclinic points persist, and are progressively destroyed with the increase in size of the dissipation. This transition, described in [23], is illustrated in figure 2.5, where, from left to right, we see how the invariant manifolds in the bottom progressively separate until we have a flow-type resonance. There is a whole sequence of homoclinic bifurcations taking place.

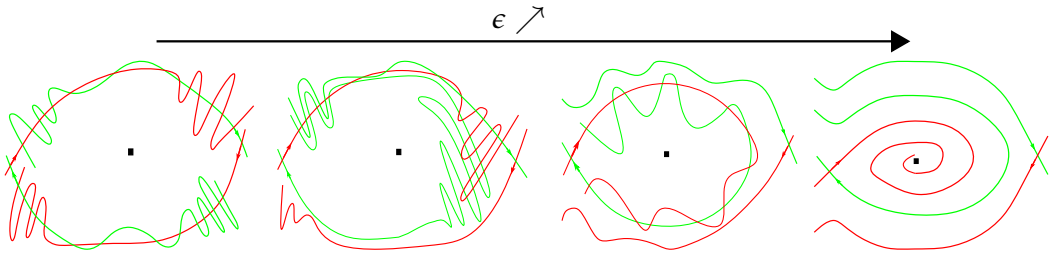

Figure 2.5: Evolution of the invariant manifolds surrounding a resonance. The left sketch represents an "almost conservative" island, and the size of the dissipation increases as we go to the right, where we have a flow-type resonance.

2.2 Coexistence of attractors and basins of attraction

If the size of the dissipation is small enough, resonances of the conservative case can persist in the dissipative scenario, such as in figures 2.2 and 2.4. Hyperbolic points keep their properties in this case, although their invariant manifolds evolve as explained in section 2.1. On the other hand, the perturbed elliptic points turn into attracting foci. Therefore, the persisting resonant structure contains a periodic attractor, and there is a coexistence of attractors since there is always an attractor where the dissipation points to.

Note that even though there are q foci in a perturbed q-periodic orbit, there is a single periodic attractor: Since points that are captured by this attractor visit all foci in the resonance, we cannot distinguish separate basins of attraction for each focus, that is, they do not have disjoint regions of the phase space where points belonging to those end captured by a determined focus. Instead, there is only a basin of attraction, and points proceed to visit all foci in the orbit.

When we are in the situation of coexistence of attractors, one may wonder which one captures the most points, and how the ratio of captured points varies in terms of ϵ. To this end, we focus on the dissipative Hénon map. Assume we have a value of the parameter $\alpha = \frac{q}{m} + \delta$, $1 \leq q < m$, $\gcd(q, m) = 1$ and a dissipative parameter ϵ such that the $q : m$ resonance still persists. In our case, we will use $\alpha = 0.21$ in order to study the 1:5 resonance, and several ϵ values in order to compare the ratio of captured points of each attractor for different sizes of dissipation. For a given α and ϵ, we have performed the following simulation:

1. We calculate two radii r_0 and r_m such that

$$|H_{\alpha,\epsilon}(x) - \mathbf{0}| < r_0 \quad \forall x \in \partial B_{r_0}(\mathbf{0}), \tag{2.7}$$

$$|H^m_{\alpha,\epsilon}(x) - x_m| < r_m \quad \forall x \in \partial B_{r_m}(x_m), \tag{2.8}$$

   that is, we calculate the radii so that the image of the points in the circumference centered at the origin (respectively, at a point x_m of the $q : m$ resonance) with radius r_0 (respectively, r_m) remain inside the circumference. This allows us to consider a point $x \in B_{r_0}(\mathbf{0})$ (respectively, $B_{r_m}(x_m)$) to be captured by the origin (respectively, the periodic foci), since it cannot escape the region enclosed by the circumference. To compute these radii, we have used the following strategy, see Appendix A.2 for details on the implementation:

   (a) Set an initial radius r^0. The first guesses for each one are $r_0^0 = (\frac{1}{2} + \epsilon)|x_m - x_0|$ for r_0 and $r_m^0 = r_0/4$ for r_m. Observe that r_0 is computed first, since our first guess for r_m employs its value.
   (b) In the k-th step, check if the corresponding inequality (either (2.7) or (2.8)) holds. If it does, set $r = r^k$. Otherwise, set $r^{k+1} = Ar^k$, where $A = 0.9$ when computing r_0 and $A = 0.95$ when calculating r_m.

2. If $\epsilon \sim 10^{-k}$, we perform $2 \cdot 10^k$ iterates on points on an invariant curve surrounding the m-order resonance in the conservative scenario. The invariant curve needs to be inside the stability domain of the conservative map (see figure 1.1) in order that points belonging to it end up captured by either the origin or the resonance.

3. We tag each initial point with a 0 if it was captured by the origin, a 1 if it is captured by the resonance or a 2 if it is not captured by either. In this case,

we perform $10^7 - 10^8$ extra iterates in order to see if the point is captured by an attractor after those iterates.

Even though the radii from step 1 guarantee that all points that fall inside the region enclosed by the circumferences do not escape under iteration, one must be careful selecting radii since:

i) The circumferences must not intersect with each other, nor with the invariant curves from which we pick initial conditions.
ii) Choosing a radius that is too small results in a lot of iterates needed in order to get inside the circumference. Our initial guesses for the radii ought to prevent this.

To save time, the radii computation is done only for $\epsilon = 5 \cdot 10^{-3}$, which is the largest value of the dissipation parameter in our simulation. Nevertheless, this will not affect our results significantly since the periodic attractor captures the least points for this value of ϵ, which means that, if r_m works for this ϵ, it will work for lower values of the dissipation parameter as well. On the other hand, the value considered for r_0 is useful for smaller sizes of dissipation since no resonance survives inside the ball of this radius around the origin for the values of ϵ considered. Thus, the radii employed in the simulation are

$$r_0 = 0.3340670, \qquad r_5 = 0.0475043. \tag{2.9}$$

Note that the smaller the dissipation parameter ϵ, the more iterates are needed to decide about the assymptotic behaviour of the initial points. Indeed, for a small dissipation parameter, points converge very slowly to an attractor, because in the conservative case they were not able to reach that region of phase space.

Point	$\mathbf{n_0}$	$\boldsymbol{\rho_0}$	$\mathbf{n_5}$	$\boldsymbol{\rho_5}$	$\mathbf{n_?}$	$\boldsymbol{\rho_?}$
$(0.683649738552201, 0.530293094929367)$	1582	0.7910	418	0.2090	0	0
$(0.696796848908974, 0.465475653404428)$	1618	0.8090	382	0.1910	0	0
$(0.709943959265747, 0.400658211879489)$	1732	0.8660	268	0.1340	0	0
$(0.723091069622521, 0.335840770354550)$	1653	0.8265	347	0.1735	0	0
$(0.736238179979294, 0.271023328829611)$	1607	0.8035	393	0.1965	0	0

Table 2.1: Comparison of the number of points of different conservative invariant curves surrounding the 1:5 resonance captured by each attractor.

To provide evidence on the robustness of the reported results, we have compared, for $\epsilon = 5 \cdot 10^{-3}$, the ratios of number of points in each curve captured between number of total points to the same ratios from outer invariant curves.

The results are presented in table 2.1, where the first column indicates the initial condition taken on the symmetry line $y = \tan(\pi\alpha)x$ of the conservative Hénon map , n_0 is the number of points captured by the origin, n_5 is the number of points captured by the 1:5 resonance, $n_?$ the number of points that are not captured by neither and ρ_0, ρ_5 and $\rho_?$ are the corresponding ratios with respect with the total number of points on each curve, $n_{tot} = 2000$, which has been chosen in order to have a uniform set of points along each curve.

We see that the ratio of number of points captured by each attractor slightly oscillates for each curve, except for the third one, which seems to have significantly more points captured by the origin than the rest. We believe that these oscillations are due to changes of the transversality of the "entrance and crossing channels" of the 5-order resonance with the invariant curve, and to the fact that we iterate a relatively small number of initial conditions. We will use the first curve to perform the simulation with other values of ϵ, whose ratios are more consistent with the ones of the other invariant curves. This invariant curve is the closest one to the 1:5 resonance depicted in figure 1.1.

ϵ	$\mathbf{n_0}$	$\boldsymbol{\rho_0}$	$\mathbf{n_5}$	$\boldsymbol{\rho_5}$	$\mathbf{n_?}$	$\boldsymbol{\rho_?}$
$5 \cdot 10^{-3}$	1582	0.7910	418	0.2090	0	0
10^{-3}	1122	0.5610	878	0.4390	0	0
$5 \cdot 10^{-4}$	1398	0.6990	602	0.3010	0	0
10^{-4}	1037	0.5185	963	0.4815	0	0
$5 \cdot 10^{-5}$	1053	0.5265	947	0.4735	0	0
10^{-5}	1148	0.5740	852	0.4260	0	0
$5 \cdot 10^{-6}$	1167	0.5835	833	0.4165	0	0
10^{-6}	1148	0.5740	848	0.4240	4	0.002
$5 \cdot 10^{-7}$	1150	0.5750	838	0.4190	12	0.006
10^{-7}	1162	0.5810	781	0.3905	57	0.0285

Table 2.2: Number of points of the invariant curve captured by each attractor, with the corresponding ratios with respect to the total number of points. The table also shows the number of points which are not captured after iteration.

In table 2.2, we show the results concerning the captured points by each attractor for values of ϵ ranging between 10^{-7} and $5 \cdot 10^{-3}$.

Furthermore, it is not until we have $\epsilon \sim 10^{-6}$ that we have points which are not captured by any attractor after iteration of the mapping. This might be caused by the persistence of additional resonances near the invariant curve for this and lesser values of ϵ, as can be observed in figure 2.6.

In figure 2.7, we have plotted the points that end at the periodic attractor and

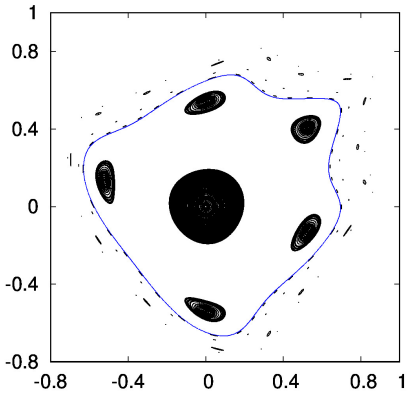

Figure 2.6: Phase space of the dissipative Hénon map for $a = 0.21$ and $\epsilon = 10^{-6}$. We have performed, a transient of 10^6 iterates for 100 initial conditions and plotted the next 10000 iterates. The invariant curve from which we pick points to perform the simulation is plotted in blue.

the origin in blue and red, respectively, as well as the circumferences of radii r_5 and r_0 surrounding each 5-periodic point and the origin, respectively. The colored dots that are found inside each circumference correspond to the last iteration of each point. Notice how, for larger values of ϵ, there are well-defined intervals on the curve, each one ending captured by either the origin or the resonance. These intervals mix up as ϵ becomes smaller, until one cannot distinguish them anymore. This has to do with the transversality between the "entrance and crossing channels" and the invariant curve and with the fact that for ϵ small enough there appear homoclinic points in the resonant structure, see 2.5.

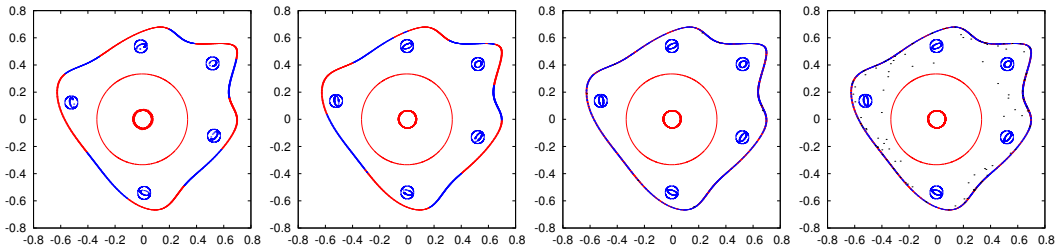

Figure 2.7: Representation of the invariant curve where a point is plotted in blue, red and black if it is captured by the resonance, the origin or it has not been captured, respectively. The final iteration is depicted in the same color. Moreover, the circumferences of radii (2.9) are depicted in red and blue, respectively. The values of ϵ are, from left to right: 10^{-3}, 10^{-4}, 10^{-6} and 10^{-7}.

2.3 Weakly-dissipative standard map

The standard map, being defined on the cylinder, allows for other kinds of dissipation to show interesting phenomena. The dissipation considered in (6) is vertical, in the sense that it points to $y = 0$. The dissipative standard map can be rewritten as [4, 5, 6, 7, 9]

$$S_{k,\epsilon,c} : \begin{pmatrix} x \\ z \end{pmatrix} \mapsto \begin{pmatrix} \bar{x} \\ \bar{y} \end{pmatrix} = \begin{pmatrix} x + \bar{y} \\ (1-\epsilon)y + \frac{k}{2\pi}\sin(2\pi x) + c \end{pmatrix}, \tag{2.10}$$

where c is known as a *drift parameter*, via the change of coordinates $\mathcal{C}(x, y) = (x, y + \omega)$ and setting $c = \epsilon\omega$. Setting $c = 0 = \omega$, we obtain the dissipative standard map studied in [20], which is the one used to obtain figure 2.4. In this case, the topology of the phase space as explained in section 2.1 and 2.2: Elliptic points turn into foci, hyperbolic points persist and their invariant manifolds evolve to "guide" points to the attractors, and there is a coexistence of attractors in the weakly-dissipative scenario. Although the topology of the manifolds surrounding the focus at $(1/2, 0)$ is different than the one of the invariant manifolds of the hyperbolic fixed point for the dissipative Hénon map, the phase spaces of both mappings are very similar.

Nevertheless, this changes when we set $\omega \neq 0$ since the frequency of $y = 0$ becomes ω. For $k = 0$, the standard map is a twist map. Therefore, we will have a periodic orbit at $y = 0$ if ω is rational, or an invariant curve if $\omega \in \mathbb{R}\backslash\mathbb{Q}$. Thus, for $k = \epsilon = 0$ and $\omega = \varphi$, we will have the *golden curve* at $y = 0$, i.e. a r.i.c. with frequency φ.

As mentioned, the phase space of the standard map is the cylinder. The topology of the phase space of a dynamical system has dynamical consequences. In the case of the cylinder, we observe that a rotational invariant curve does not trap any region of the phase space, thus does not contradicting equation 2.2. However, two r.i.c.'s do enclose an area on the cylinder. Therefore, the presence of two of these objects is impossible in the dissipative case, but, with a suitable choice of parameters, a single r.i.c. might be able to survive.

Indeed, when considering $\epsilon > 0$, the golden curve mentioned above persists, and it becomes an attractor. When the dissipation is strong enough (e.g. $\epsilon = 0.05$), it is the only remaining attractor. For (2.10), it is located at $y = \frac{c}{\epsilon}$. Thus, it goes to infinity as $\epsilon \to 0$. In our formulation (6), this attractor remains near $y = 0$.

In general, for $k \neq 0$ we will expect an invariant object with frequency ω near $y = 0$ for any value of $\epsilon \geq 0$ considered. In particular, if $\omega = \varphi$, the attractor has frequency equal to the golden mean. This is also true for the (2.10), although to have an invariant object with rotation number ω in this case, given ϵ we must set the drift parameter to $c = \epsilon\omega$.

2.3.1 Golden curve breakdown

One might wonder what happens to the golden curve when changing parameters. We know that it persists for k small enough as a consequence of theorem 1.2.2. Indeed, it persists until $k = k_G$. Here, we investigate its persistence when adding dissipation. For this purpose, throughout this section we will set $\omega = \varphi$, and see, for a given k, what dissipation parameter ϵ is needed in order to break the golden curve.

We will look for the golden curve breakdown for two different starting values of k: The first one is $k = 0.628$, whereas the second one is $k = 0.92$. The reason behind this election is the distance of each parameter to the Greene parameter k_G (see section 1.2.2). Indeed, we know that there are no invariant curves for $k > k_G$, and thus we require that k is below this threshold. Moreover, for values of k closer to k_G, we expect the breakdown of the golden curve to occur sooner, that is, for a smaller value of ϵ.

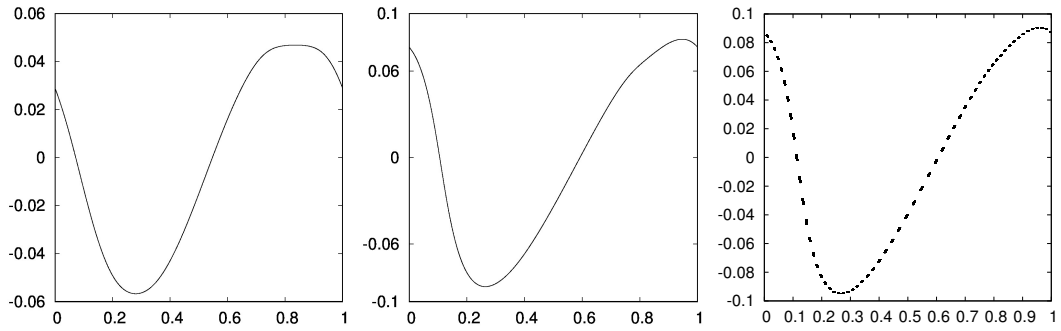

Figure 2.8: Golden curve of the dissipative standard map for $k = 0.628$, $\omega = \varphi$. From left to right: $\epsilon = 0.016, 0.8, 0.9$.

In all figures displayed in this section, we have plotted 10000 iterates of 100 initial conditions after a transient of 10^6 iterates in order to get closer to the attractor.

Before discussing the results, we must take into account that we deal with a *quasiattractor*, that is, an attractor that is very sensitive to perturbation, for which is very difficult to distinguish between, for example, an invariant curve or a periodic orbit of very high period or even a strange attractor. Hence, when we claim in the following that we see a concrete type of attraction, such assertion is to be understood under numerical and observational limitations.

In figure 2.8, the phase space of the standard map for $k = 0.628$ is depicted for different values of ϵ. We see that the curve persists for values of ϵ up to 0.8, but all resonant structures are destroyed. As the dissipative parameter increases, the curve is progressively deformed, as one can see from comparing the left and

middle of figure 2.8. When we further increase the parameter, we see that the curve is destroyed and a periodic orbit of high period takes its place, as seen on the right of figure 2.8.

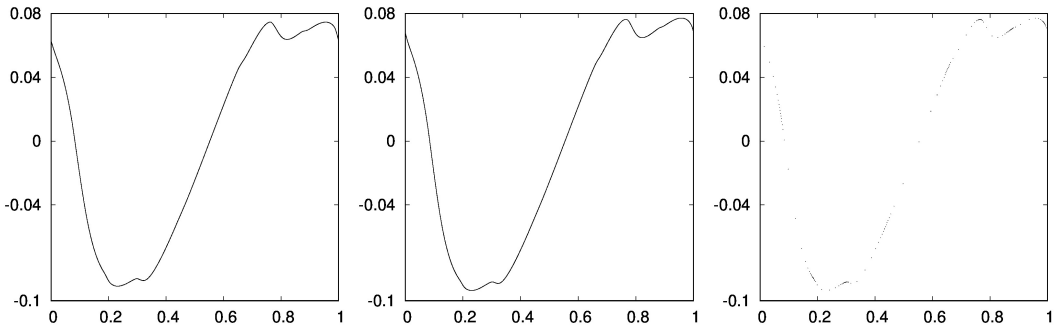

Figure 2.9: Golden curve of the dissipative standard map for $k = 0.9$ and $\omega = \varphi$. From left to right, the values of ϵ are 0.2, 0.24991 and 0.24993, respectively.

On the other hand, in figure 2.9 we see the dissipative standard map for the values $k = 0.92$ and $\omega = \varphi$. We see how, even if k is close to k_G, the golden curve persists up until very large values of the dissipation parameter ($\epsilon \simeq 0.2$). We see that the breakdown of the curve occurs for a value $0.24991 < \epsilon < 0.24993$, which is clear from looking at the middle and right of figure 2.9.

2.3.2 Exploring other kinds of attractors

We have seen how, for $\omega \in \mathbb{R}\backslash\mathbb{Q}$, the dissipative standard map can have an attracting rotational invariant curve, although it is eventually destroyed by the dissipation. Nevertheless, the attractor of this mapping can be different from an invariant curve.

Indeed, we have seen how for, given $\omega = \varphi$, the values $k = 0.92$ and $\epsilon = 0.2$ give rise to an invariant curve near $y = 0$. As we have previously mentioned, these invariant objects are very sensitive to perturbation, leading to a quasiattractor scenario: We do not know with certainty if we are looking at an invariant curve or a periodic orbit, since a small change of parameters would change the attractor from a periodic object to a quasiperiodic one (e.g. an invariant curve). This is made clear in figure 2.10. For $k = \frac{\pi}{10}$ and $\epsilon = 0.3$, we have

i) a 2-periodic orbit for $\omega = 0.507\hat{6}$ and
ii) an invariant curve for $\omega = 0.5077$.

If we now consider $\frac{k}{2\pi} = 0.145$ and $\epsilon = \frac{\varphi+1}{10}$, we arrive at a striking result: The invariant curve is folding onto itself at all scales, as seen in figure 2.11. Even

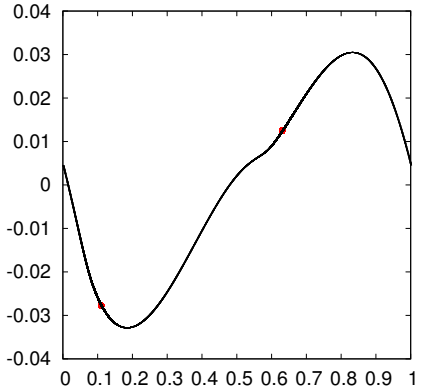

Figure 2.10: Quasiattraction scenario for the dissipative standard map.

though it might seem that we are looking at an invariant curve at first, in fact we are not: The curve is a *strange attractor* with frequency φ. Strange attractors are invariant objects with chaotic behaviour. The difference between a strange attractor and an invariant curve comes by how the points on each attractor behave under iteration: An invariant curve moves its iterates quasiperiodically, whereas a strange attractor does not.

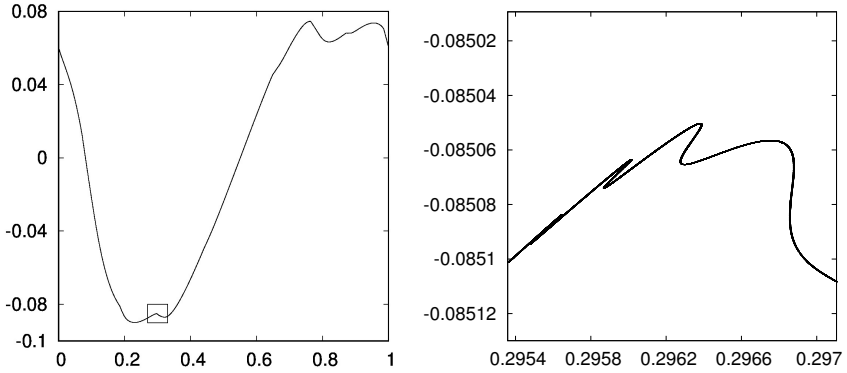

Figure 2.11: Strange attractor with frequency φ of the dissipative standard map.

On the right of figure 2.11 there is a close-up on one of the foldings, surrounded by a square on the left of the same figure. If we were to close in even more, and with infinite numerical precision, we would see that this folding occurs infinitely many times at all scales. However, we are again facing a quasiattractor scenario: Due to limited numerical precision, we cannot be certain that we are looking at a strange attractor or at a periodic orbit of high-period. What we do know is that if we slightly moved the parameters, we would get either. Despite that, we can

assure it is not an invariant curve, since the latter needs to be smooth and must not have foldings.

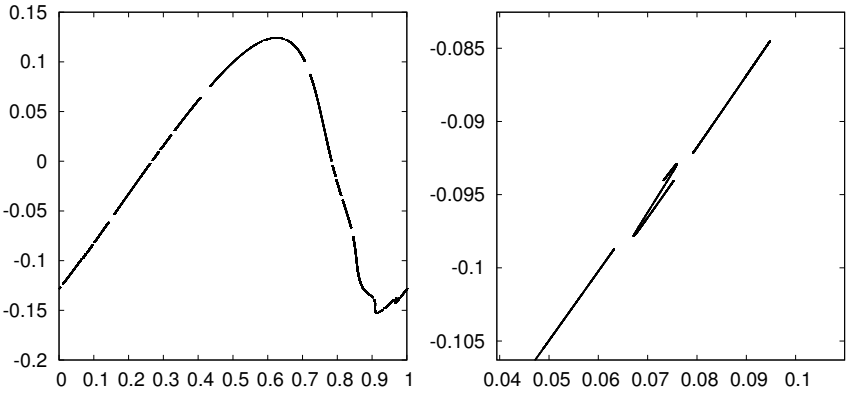

Figure 2.12: Strange attractor with periodic components.

This is not the only set of parameters for which we have a strange attractor. In fact, there is one with frequency $\omega \simeq 0.2040816327$ when $k \simeq 0.7539822369$ and $\epsilon = 0.49$. Nevertheless, the following combination of parameters looks more interesting: Consider $k \simeq 0.7665486075$, $\epsilon = 0.5$ and $\omega = 0.2$. The result is depicted in figure 2.12: The system has a strange attractor with periodic components. If we were to perturb the system, this attractor would either become a connected strange attractor (as in figure 2.11) with frequency ω or a periodic orbit: Again, we are presented with a quasiattractor escenario.

If instead of considering our formulation of the dissipative standard map we used

$$S_{k,\epsilon,\omega} : \begin{pmatrix} x \\ y \end{pmatrix} \mapsto \begin{pmatrix} \bar{x} \\ \bar{y} \end{pmatrix} = \begin{pmatrix} x + \bar{y} + \omega \\ (1-\epsilon)y + \frac{k}{2\pi} V(2\pi x) \end{pmatrix}, \tag{2.11}$$

where $V(2\pi x)$ is an arbitrary periodic function, one could observe larger strange attractors. For more information on this version of the standard map, we refer the reader to [6, 7].

Understanding the bifurcations leading to the different presented attractors is far beyond the goals of this work. Moreover, there are many open questions regarding to all the phenomena shown in the previous illustrations of dissipative and weakly-dissipative maps, see comments in chapter 3.

Chapter 3

Summary, conclusions and outlook

In this work, we have studied the effect of dissipation on analytic area-preserving maps. The transition from the conservative case to the dissipative one is closely related to the structure of the phase space of the former. To better understand this, in chapter 1 we studied the dynamics of area-preserving maps, using the Hénon map and the standard map as paradigmatic examples.

We saw that the dynamics of an APM around hyperbolic fixed points is topologically conjugated to that of the related linear system (theorem 1.1.1), and that these points have global and unique unstable and stable manifolds (theorem 1.1.2) which deeply affect the dynamics of the map. We also implemented a simple algorithm for their computation, and explained how chaos arises in APMs via the horseshoe map, which has chaotic dynamics, and how this system is present in an APM due to transversal intersections of the invariant manifolds (theorem 1.3.3), which form homoclinic and heteroclinic tangles.

Around an elliptic fixed point, theorem 1.1.1 does not apply, and so normal forms are required in order to simplify the expression of an APM around that kind of point. In particular, Birkhoff normal forms are useful since the resulting expression is a twist map, which has a twist interval where each orbit has a frequency in this interval. In addition, the twist condition is essential for the most important theorems of chapter 1: The Moser Twist theorem (theorem 1.2.2), which guarantees the persistence of an invariant curve if the perturbation is small enough, and the Poincaré-Birkhoff theorem 1.2.3, which ensures the persistence of periodic orbits under perturbation.

In the dissipative case, we saw how the conservative structure crumbles: All invariant curves are destroyed (save for a maximum of one on the standard map), and elliptic points turn into attracting foci, where the long-term dynamics of the

system is concentrated. If the dissipation is not large enough, some periodic orbits survive, even though the elliptic orbits turn into foci as well.

Hyperbolic points persist if the dissipation is not too large, but their invariant manifolds disengage: Homoclinic and heteroclinic points of the conservative resonant structure disappear as the dissipation grows larger. The invariant manifolds now have the role of guiding points closer to the attractor.

We also studied their topology, which is different depending on the hyperbolic point considered: We saw that the invariant manifolds hyperbolic fixed points of the standard map not located at $y = 0$ have the same topology as the resonances of both the same map and the Hénon map, whereas the manifolds surrounding the elliptic points at $(1/2, 0)$ for the standard map and the origin for the Hénon map are different from each other and also differ from the ones mentioned previously.

We saw how, for both systems, there is a coexistence of attractors if the value of the dissipation parameter is small enough. Indeed, if a resonant structure persists, its elliptic points turn into foci which also attract points. This leads to a coexistence of an attracting focus and a periodic attractor.

To see how the number of points captured varies in terms of ϵ, we performed an experiment on the dissipative Hénon map. The experiment consists on counting how many points from an invariant curve of the conservative case are captured by each of the persistent attractors.

Finally, we did a numerical exploration of the dissipative standard map, where the dissipation applied allows for a single rotational invariant curve to survive. Furthermore, it has an additional parameter ω, which sets the frequency of the attractor near $y = 0$. This allows this attractor to be a r.i.c., a periodic orbit or a strange attractor (including one with periodic components), which is an attractor with chaotic dynamics.

There are still many open questions concerning the transition from conservative to weakly-dissipative dynamics. For example, any small dissipation creates basins of attraction associated to the different attractors that coexist. These basins of attraction have positive measure, hence the probability of capture by each attractor is non-zero. How do these probabilities behave when ϵ tends to zero? We saw, in the experiment of section 2.2, that the probability of capture by the periodic attractor and the one at the origin seems to remain bounded from zero for the range of ϵ explored. What happens for small values of ϵ?

Related to the previous questions, we note that the homoclinic structure of the conservative island is recovered when ϵ tends to zero (see figure 2.5). Hence, the invariant manifolds no longer define “entrance and crossing channels", and the transients become more and more chaotic (although the long term dynamics tends to the attractors). How are these dissipative chaotic transients related to the

conservative chaos?

Furthermore, the concrete types of dissipation studied in this work are rather simple. Other ways of adding dissipation can lead to different resonant structures (due to different bifurcations). Also, in many real processes, the dissipation stress decays through time. How do these effects change the probability of capture by the coexistent attractors?

To conclude, we can say that this work simply highlights the need of further investigations on the transition from conservative to dissipative dynamics while emphasizing the importance of this setting in real-life applications.

Appendix A

Implemented codes

A.1 Computation of invariant manifolds

Here we present the code, written in C++, employed to compute the invariant manifolds of hyperbolic points. The algorithm, which is coded from line 198 to line 263, is explained in section 1.1. We include the implementation of the map, its inverse and the computation of the fundamental domain.

```
1  #include <iostream>
2  #include <fstream>
3  #include <cmath>
4  #include <vector>
5  #include <cstdio>
6  #include <sstream>
7
8  using namespace std;
9
10 //Tolerance
11
12 const double dmax = 1.e-4; //Maximum distance between iterations
13 const double dzmin = 1.e-14; //Minimum distance between initial conditions
14
15 double sq(double x){return x*x;}
16
17 double min(double x, double y){
18
19    if (x <= y)
20    return x;
21    else
22    return y;
23
24 }
25
26 double norm(vector <double> x){return sqrt(sq(x[0]) + sq(x[1]));}
27
```

```
28 //Computes the distance between two points: It needs to be adapted for the
       standard map, since it is defined on the cylinder.
29
30 double dist(vector <double> x, vector <double> y){
31
32 vector <double> v(2);
33
34    v[0] = y[0] - x[0];
35    v[1] = y[1] - x[1];
36
37    return norm(v);
38
39 }
40
41 /*Map: Computes the image of a point x under the map (in this case the Hénon
       map), with parameters alpha and eps. Change for the expression of the
       standard map if one wants to compute the invariant manifolds of that
       mapping.*/
42
43 vector <double> map(vector <double> x, double alpha, double eps){
44
45    vector <double> H(2);
46    double c=cos(2*M_PI*alpha), s=sin(2*M_PI*alpha), x2 = sq(x[0]);
47
48    H[0] = (1 - eps)*(c*x[0] - s*(x[1] - x2));
49    H[1] = (1 - eps)*(s*x[0] + c*(x[1] - x2));
50
51 return H;
52
53 }
54
55 //Inverse mapping
56
57 vector <double> inverse(vector <double> x, double alpha, double eps){
58
59    vector <double> inv(2);
60    double c=cos(2*M_PI*alpha), s=sin(2*M_PI*alpha), xaux = x[0]/(1 - eps),
          yaux =   x[1]/(1 - eps);
61
62    inv[0] = c*xaux + s*yaux;
63    inv[1] = -s*xaux + c*yaux + sq(c*xaux + s*yaux);
64
65    return inv;
66
67 }
68
69 int main(){
70
71    //Input
72
73    double alpha, eps, lmax;
74
75    cerr << "Value␣of␣the␣parameter?" << endl;
76    cin >> alpha;
77
78    cerr << "Value␣of␣the␣dissipative␣parameter?" << endl;
```

```
79    cin >> eps;
80
81    double c = cos(2*M_PI*alpha), s = sin(2*M_PI*alpha), t = tan(M_PI*alpha),
          mu = 1 - eps;
82
83    /*
84    In order to compute invariant manifolds in the dissipative case, one must
          substitute:
85
86    - Eigenvalue and eigenvector. Moreover, the lack of reversors implies that
          the program must be executed twice: once per invariant manifold.
87    - Use the function map (inverse) to compute the unstable (stable) manifold.
88    */
89
90    //Hyperbolic fixed point
91
92    vector <double> fix(2);
93
94    fix[0] = (1 - 2*c*mu + sq(mu))/(mu*s);
95    fix[1] = fix[0]*(mu - c)/s;
96
97    //Eigenvalue and normalised eigenvector of the (un)stable manifold
98
99    double sum = c + 2*s*t, lambda;
100
101   if (eps == 0)
102      lambda = sum + sqrt(sq(sum) - 1);
103   else{
104
105      cerr << "Eigenvalue?" << endl;
106      cin >> lambda;
107
108   }
109
110   vector <double> vep(2);
111
112   if (eps == 0){
113
114      vep[0] = -1;
115      vep[1] = sqrt(sq(sum) - 1)/s - 2*t;
116
117   } else{
118
119      cerr << "Eigenvector?" << endl;
120      cin >> vep[0] >> vep[1];
121
122   }
123
124   double modul  = norm(vep);
125
126   vep[0] /= modul;
127   vep[1] /= modul;
128
129   ofstream output;
130   stringstream ss;
131
```

```
132    if (eps == 0)
133       ss <<"H-" << alpha << "-manifold.dat";
134
135    else{
136
137       if (lambda > 1)
138          ss <<"H-" << alpha << "_" << eps << "-unst.dat";
139       else
140          ss <<"H-" << alpha << "_" << eps << "-st.dat";
141
142    }
143
144    string filename = ss.str();
145    output.open(filename);
146
147    //For the computation of the stable manifold we have to consider the
           inverse of the eigenvalue
148
149    if (lambda < 1)
150       lambda = 1./lambda;
151
152    cerr << "Manifold␣length?" << endl;
153    cin >> lmax;
154
155    /* Fundamental domain (z0/lambda, z0) (C. Simó notation): We choose z0 when
           the distance F(x(z))-x(lambda*z) <10^-14*/
156
157    for (int i = 0; i < 2; i++){
158
159       if (i == 1){
160
161          cerr << "Longitud␣de␣l'altra␣branca?" << endl;
162          cin >> lmax;
163          vep[0] = -vep[0];
164          vep[1] = -vep[1];
165
166       }
167
168       int n = 0;
169       double z0;
170       vector <double> x(2), linear(2);
171
172       do{
173
174          n++;
175          z0 = pow(10, -n);
176
177          x[0] = fix[0] + z0*vep[0];
178          x[1] = fix[1] + z0*vep[1];
179
180          linear[0] = fix[0] + lambda*z0*vep[0];
181          linear[1] = fix[1] + lambda*z0*vep[1];
182
183       } while (dist(map(x, alpha, eps), linear) >= dzmin);
184
185       z0 = min(z0, 1.e-8);
```

```
186       vector <double> aux(2);
187
188       aux[0] = fix[0] + z0*vep[0];
189       aux[1] = fix[1] + z0*vep[1];
190
191       double z = z0/lambda, dz = z0, length = 0., fac = 1.;
192       bool okay = true;
193
194       ////Manifold computation via the linear parameterization algorithm
195
196       output << "#" << endl;
197
198       do{
199
200          int nit = 0;
201          double zaux = z;
202
203          while (fabs(zaux) > z0){
204
205             zaux /= lambda;
206             nit++;
207
208          }
209
210          x[0] = fix[0] + zaux*vep[0];
211          x[1] = fix[1] + zaux*vep[1];
212
213          for(int i = 0; i < nit; i++)
214             x = henon(x, alpha, eps);
215
216          double d = dist(x, aux);
217
218          if (d < dmax){
219
220             if(d < dzmin){
221
222                okay = false;
223                cerr << "No avanço" << endl;
224
225             }
226
227             output << setprecision(15) << x[0] << "\t" << setprecision(15) <<
                    x[1] << endl;
228             aux = x;
229             length += d;
230             nit++;
231
232             fac = min(1.5, 0.75*dmax/d);
233             dz *= fac;
234             z += dz;
235
236             if(fabs(dz) <= dzmin){
237
238                okay = false;
239                cerr << "dz petit" << endl;
240
```

```
241             }
242
243         } else{
244
245             z -= dz;
246             fac = 0.75*dmax/d;
247             dz *= fac;
248             z += dz;
249
250             if(fabs(dz) <= dzmin){
251
252                 okay = false;
253                 cerr << "dz petit" << endl;
254
255             }
256
257         }
258
259     } while (okay == true && length < lmax);
260
261     output << endl;
262
263 }
264
265 output.close();
266
267 }
```

A.2 Computation of the number of points captured by attractors

The codes presented here, both written in C++, correspond to the simulation performed in section 2.2. The first code is used to compute the radii, whereas the second one calculates the number of points captured by each attractor, as well as the ratios with respect to the total number of points.

```
1
2 #include <iostream>
3 #include <fstream>
4 #include <cmath>
5 #include <vector>
6 #include <cstdio>
7
8 using namespace std;
9
10 double alpha = 0.21, c = cos(2*M_PI*alpha), s = sin(2*M_PI*alpha);
11 double eps = 5e-3;
12
13 double sq(double x){return x*x;}
14
15 double min(double x, double y){
16
```

```
17     if (x <= y)
18        return x;
19     else
20        return y;
21 
22 }
23 
24 double norm(double* x){return sqrt(sq(x[0]) + sq(x[1]));}
25 
26 double dist(double* x, double* y){
27 
28     double v[2];
29 
30     v[0] = y[0] - x[0];
31     v[1] = y[1] - x[1];
32 
33     return norm(v);
34 
35 }
36 
37 //Change from polar coordinates to cartesian coordinates
38 
39 void polar(double r, double theta, double* x){
40 
41     x[0] = r*cos(theta);
42     x[1] = r*sin(theta);
43 
44 }
45 
46 //Hénon map defined on R^2
47 
48 void henon(double* x, double* y){
49 
50     double x2 = sq(x[0]);
51 
52     y[0] = (1 - eps)*(c*x[0] - s*(x[1] - x2));
53     y[1] = (1 - eps)*(s*x[0] + c*(x[1] - x2));
54     x[0] = y[0];
55     x[1] = y[1];
56 
57 }
58 
59 int main(){
60 
61     //Input
62 
63     int per, npt, nit;
64     double xper[2];
65 
66     cerr << "Period␣of␣the␣orbit?" << endl;
67     cin >> per;
68 
69     cerr << "Coordinates␣of␣a␣" << per << "-periodic␣point?" << endl;
70     cin >> xper[0] >> xper[1];
71 
72     cerr << "Number␣of␣initial␣conditions?" << endl;
```

```
73    cin >> npt;
74
75    cerr << "Number␣of␣iterations?" << endl;
76    cin >> nit;
77
78    ofstream output;
79    output.open("basin.in");
80
81    //Computation of the radii
82
83    double theta;
84    double x[2], aux[2];
85
86    //r0: Cercle surrounding the origin
87
88    int n0 = 0;
89    double r0 = (0.5 + eps)*norm(xper);
90
91    while (n0 < npt){
92
93       n0 = 0;
94
95       for (int i = 0; i < npt; i++){
96
97          theta = 2*M_PI*i/npt;
98          polar(r0, theta, x);
99
100         for (int j = 0; j < nit; j++)
101            henon(x, aux);
102
103         if (norm(x) < r0)
104            n0++;
105
106      }
107
108      if (n0 < npt)
109         r0 *= 0.9;
110
111   }
112
113   //rper: Cercle surrounding each periodic point
114
115   int nper = 0;
116   double rper = 0.25*r0;
117
118   while (nper < npt){
119
120      nper = 0;
121
122      for (int i = 0; i < npt; i++){
123
124         theta = 2*M_PI*i/npt;
125         polar(rper, theta, x);
126         x[0] += xper[0];
127         x[1] += xper[1];
128
```

```
129          for (int j = 0; j < nit; j++)
130             for (int m = 1; m <= per; m++)
131                henon(x, aux);
132
133          if (dist(xper, x) < rper)
134             nper++;
135
136       }
137
138       if (nper < npt)
139          rper *= 0.95;
140
141    }
142
143    //Results: They are printed on the file basin.in, which is the input file
           for the program basin.cpp
144
145    output << per << endl;
146    output << setprecision(15) << xper[0] << "\t" << setprecision(15) << xper
           [1] << endl;
147    output << 2*pow(10,-floor(log10(eps))) << endl;
148    output << 1e5 << endl;
149    output << setprecision(15) << r0 << endl;
150    output << setprecision(15) << rper << endl;
151    output << "p" << endl;
152    output << "basin_" << eps << endl;
153
154    output.close();
155
156 }
```

```
1  #include <iostream>
2  #include <fstream>
3  #include <cmath>
4  #include <vector>
5
6  using namespace std;
7
8  double alpha = 0.21, c = cos(2*M_PI*alpha), s = sin(2*M_PI*alpha);
9  double eps = 5e-4;
10
11 double sq(double x){return x*x;}
12
13 double min(double x, double y){
14
15    if (x <= y)
16    return x;
17    else
18    return y;
19
20 }
21
22 double norm(double* x){return sqrt(sq(x[0]) + sq(x[1]));}
23
24 double dist(double* x, double* y){
25
```

```
26     double v[2];
27 
28     v[0] = y[0] - x[0];
29     v[1] = y[1] - x[1];
30 
31     return norm(v);
32 
33 }
34 
35 //Hénon map defined on R^2
36 
37 void henon(double* x, double* y){
38 
39     double x2 = sq(x[0]);
40 
41     y[0] = (1 - eps)*(c*x[0] - s*(x[1] - x2));
42     y[1] = (1 - eps)*(s*x[0] + c*(x[1] - x2));
43 
44     x[0] = y[0];
45     x[1] = y[1];
46 
47 }
48 
49 int main(){
50 
51     //Input
52 
53     int per;
54     double xper[2];
55     double nit, nitaux, r0, rper;
56     string infile, outfile;
57 
58     cerr << "Period␣of␣the␣orbit?" << endl;
59     cin >> per;
60 
61     cerr << "Coordinates␣of␣a␣" << per << "-periodic␣point?" << endl;
62     cin >> xper[0] >> xper[1];
63 
64     cerr << "Number␣of␣iterations?" << endl;
65     cin >> nit;
66 
67     cerr << "Number␣of␣iterations␣if␣there␣is␣not␣convergence?" << endl;
68     cin >> nitaux;
69 
70     cerr << "Radius␣surrounding␣the␣origin?" << endl;
71     cin >> r0;
72 
73     cerr << "Radius␣surrounding␣the␣" << per << "-periodic␣points?" << endl;
74     cin >> rper;
75 
76     cerr << "Input␣file?" << endl;
77     cin >> infile;
78 
79     cerr << "Output␣file?" << endl;
80     cin >> outfile;
81 
```

```
82    infile += ".dat";
83    outfile += ".dat";
84    ifstream input;
85    ofstream output;
86    input.open(infile);
87    output.open(outfile);
88
89    //Computation of number of points captured by each attractor
90
91    int npt = 0, n0 = 0, nper = 0;
92    double x[2], aux[2], auxper[2];
93
94    while (input >> x[0] >> x[1]){
95
96       npt++;
97       output << x[0] << "\t" << x[1] << "\t";
98
99       double m = 0;
100      while (m < nit){
101
102         henon(x, aux);
103         m++;
104      }
105
106      bool decided = false;
107      double notdecided = 0;
108
109      while (decided == false){
110
111         if (norm(x) < r0){
112
113            n0++;
114            decided = true;
115            output << x[0] << "\t" << x[1] << "\t" << 0 << endl;
116
117         } else{
118
119            int m = 1;
120            auxper[0] = x[0];
121            auxper[1] = x[1];
122            while (m <= per && decided == false){
123
124               if(dist(auxper, xper) < rper){
125
126                  nper++;
127                  decided = true;
128                  output << x[0] << "\t" << x[1] << "\t" << 1 << endl;
129
130               } else{
131
132                  henon(auxper, aux);
133                  m++;
134
135               }
136
137            }
```

```
138
139          }
140
141          if (decided == false){
142
143             if (notdecided < 1.e8/nitaux){
144
145                notdecided++;
146                for (int i = 0; i < nitaux; i++)
147                   henon(x, aux);
148
149             } else{
150
151                output << x[0] << "\t" << x[1] << "\t" << 2 << endl;
152                decided = true;
153
154             }
155
156          }
157
158       }
159
160    }
161
162    int nesc = npt - (n0 + nper);
163    double p_0 = (double) n0/npt, p_per = (double) nper/npt, p_esc = (double)
           nesc/npt;
164    output << "#eps␣r0␣rper␣n0␣p_0␣nper␣p_per␣nesc␣p_esc␣npt" << endl;
165    output << "#" << eps << "␣" << r0 << "␣" << rper << "␣" << n0 << "␣" << p_0
           << "␣" << nper << "␣" << p_per << "␣" << nesc << "␣" << p_esc << "␣"
           << npt << endl;
166    input.close();
167    output.close();
168
169 }
```

Bibliography

[1] V.I. Arnold, V.V. Kozlov, and A.I. Neishtadt. *Mathematical aspects of classical and celestial mechanics. Dynamical Systems III.* Third edition. Encyclopaedia of Mathematical Sciences, 3. Springer-Verlag, 2006.

[2] D.K. Arrowsmith and C.M. Place. *An introduction to dynamical systems*. Cambridge University Press, Cambridge, 1990.

[3] P. Berger and D. Turaev. *On Herman's Positive Entropy Conjecture*. arXiv:1704.02473 [math.DS], 2017.

[4] R. Calleja, A. Celletti. Breakdown of invariant attractors for the dissipative standard map. *Chaos*, 20, 2010.

[5] R. Calleja, A. Celletti and R. de la Llave. *KAM estimates for the dissipative standard map*. arXiv:2002.10647 [math.DS], 2020.

[6] A. Celletti, C. Froeschlé and E. Lega. Dissipative and weakly-dissipative regimes in nearly-integrable mappings. *Discrete and Continuous Dynamical Systems* 16, 2006.

[7] A. Celletti. *Weakly dissipative systems in Celestial Mechanics*. In: Benest D., Froeschle C., Lega E. (eds) Topics in Gravitational Dynamics. Lecture Notes in Physics, vol 729. Springer, Berlin, Heidelberg, 2007.

[8] B.V. Chirikov. A Universal Instability of Many-Dimensional Oscillator System. *Phys. Rep.*, 52: 264-379, 1979.

[9] S. Di Ruzza. *Some results on the dynamics of conservative and dissipative systems with applications to Celestial Mechanics*. Università degli Studi di Roma "La Sapienza", 2010.

[10] E. Fontich and C. Simó (1990). The splitting of separatrices for analytic diffeomorphisms. *Ergodic Theory and Dynamical Systems*, 10(2): 295-318, 1990.

[11] J. M. Greene. *A method for determining a stochastic transition*. University of Princeton, New Jersey, 1978.

[12] J. Guckenheimer and P. Holmes. *Nonlinear Oscillations, Dynamical Systems, and Bifurcations of Vector Fields*. Ed. Springer. Applied natural sciences, 42, 1997.

[13] A. Haro, M. Canadell J.L. Figueras, A. Luque and J.M. Mondelo. *The parameterization method for invariant manifolds*. Applied Mathematical Sciences, 195. Springer, 2016.

[14] M. Hénon. Numerical study of quadratic maps. *Quarterly of applied mathematics*, 3, XXVII: 291-311, 1969.

[15] M. Hénon. A Two Dimensional Mapping with a Strange Attractor. *Commun. Math. Phys.*, 50: 69-77, 1976.

[16] M. Herman. Some open problems in dynamical systems. *Documenta Mathematica*: 797-808, 1998.

[17] M. W. Hirsch, S. Smale and R. L. Devaney. *Differential Equations, Dynamical Systems & An Introduction to Chaos*. 2nd edition. Academic Press, 2013.

[18] A. Katok and B. Hasselblatt. *A First Course in Dynamics with a panorama of recent developments*. Cambridge University Press, 2003.

[19] J. Palis Jr. On Morse-Smale dynamical systems. *Topology*, 8: 385-404, 1969.

[20] G. Schmidt and B. W. Wang. Dissipative standard map, *Phys. Rev. A*, 32(5): 2994-2999, 1985.

[21] C.L. Siegel and J.K. Moser. *Lectures on Celestial Mechanics*. Springer-Verlag, 1971.

[22] C. Simó. *On the Analytical and Numerical Approximation of Invariant Manifolds*. Les Méthodes Modernes de la Mecánique Céleste (Course given at Goutelas, France, 1989), D. Benest and C. Froeschlé (eds.), pp. 285-329, Editions Frontières, Paris, 1990.

[23] C. Simó, A. Vieiro. Planar Radial Weakly-Dissipative Diffeomorphisms. *Chaos*, 20(4): 1-18, 2010.

[24] C. Simó. Aplicacions quadràtiques que preserven l'àrea a $\mathbb{R}^2$. *Butlletí de la Societat Catalana de Matemàtiques*, 29(1): 77-108, 2014.

[25] S. Smale. Diffeomorphisms with many periodic points. *Differential and Combinatorial Topology*: 63-80. Princeton Univ. Press, Princeton N.J., 1965.

[26] J. Sotomayor. *Lições de equações diferenciais ordinárias*. Río de Janeiro: Instituto de Matemática Pura e Aplicada, CNP, 1979.

[27] A. Vieiro. *Study of the effect of conservative and weakly dissipative perturbations on symplectic maps and Hamiltonian systems*. Universitat de Barcelona, 2009.

[28] S. Wiggins. *Global bifurcation and Chaos - Analytical methods*. Springer-Verlag, New-York, Heidelberg, Berlin, 1988.